Friedrich-Alexander-Universität
Naturwissenschaftliche Fakultät

Master's Thesis
in Physics

RNO-G's Perspective on Wind - Power Generation and Background Tagging

Pascal Schriefer

Supervisor: Prof. Dr. Anna Nelles

Erlangen Centre for Astroparticle Physics

Submission date: 29.10.2025

Abstract

In this thesis, the potential of and the hardships posed by high wind speeds for the Radio Neutrino Observatory in Greenland (RNO-G) are examined. The multiple, remote stations of the detector must generate their own power as a centralised energy distribution is not possible. While during the summer solar panels can reliably supply them, in the winter months, the sun does not rise above the horizon. Wind turbines are ideal in this situation, as wind speeds regularly exceed 6-7 m/s. However, the extreme cold and the wind itself present several challenges for the detector. As the temperature very rarely rises above 0 °C, the turbines are often frozen shut. Additionally, during those high wind speed periods, the detector measures significantly higher rates of radio pulses, which are currently attributed to the Triboelectric effect.

In this work, a local station that replicates the power system of the RNO-G detector stations is built at the Erlangen Centre for Astroparticle Physics (ECAP) to serve as a testing ground for new software and technology. When examining the available turbines in Greenland, it shows they are operating within expectations based on previous wind-tunnel tests. At the transition from summer to winter, based on calculations, stations 11 and 13 would have lost 1-5 days in uptime if they had not been equipped with a turbine, while they could have been up for about half a month longer if their power draw was reduced by 10 W (about 30 %).

Secondly, a glaciophone is used to record acoustic noise at detector station 13 to test whether the wind-induced radio pulses are accompanied by an acoustic effect. The frequency analysis recordings show different results for the two runs performed. The first one shows a higher pitch for the maximum compared to the second one, which is most probably caused by the protective plastic bag used during run No.1 only. Both runs show a clear correlation between wind speed and acoustic noise; however, the relation between the trigger rate of the station and both wind velocity and the acoustic signal is not apparent. The analysis of the timing between wind speed and trigger rate increase points to a delay of about 2.8 hours (wind speed increase preceding the trigger rate spike).

Contents

1 Introduction

Currently, the most powerful particle accelerator, the LHC in Switzerland, is technologically limited to a collision energy of 14 TeV [1]. Research focusing on any energy scale beyond this needs to be conducted through analysing naturally occurring, astrophysical phenomena, which not only encode information about particle physics but astrophysics as well. Even though galactic sources emit many kinds of messengers, which are way easier to detect, like electromagnetic radiation or cosmic rays (such as protons, electrons, or helium cores), the unique properties of neutrinos make them essentially required to fully understand the extreme conditions, such as in the centre of the sun or the middle of supernovae. Neutrinos are neither perturbed by any electromagnetic fields, due to their lack of electric charge, nor are they attenuated like gamma-rays (γ-rays) because of their low interaction probability with other matter. This means that the neutrino flux is the only source of information that points directly to the source of its creation, allowing us to glimpse into the inner workings of astrophysical objects. There exist many models of how particles can be accelerated in such objects, among others, shock acceleration [2] and magnetic reconnection [3]. However, high- and ultra-high energy neutrinos ($20\,\mathrm{GeV} \lesssim E_\nu \lesssim 10\,\mathrm{PeV}$ and $E_\nu \gtrsim 10\,\mathrm{PeV}$ respectively) are most likely not accelerated themselves but are generated in collisions of accelerated hadrons with a target. These collisions create mesons which are not stable and decay, creating neutrinos in the process. Locating the sources for and discovering the principle behind the acceleration of particles beyond energies achievable on Earth would improve our understanding of particle and astrophysics immensely. After travelling through space in a straight line from the source to Earth, neutrinos induce particle showers in the detector medium, producing many secondary particles. This cascade of particles generates radio signals in two different ways - the geomagnetic and the Askaryan (charge-excess) effect. With the geomagnetic effect, differently charged particles are separated due to the Lorentz force in Earth's magnetic field. However, this process is negligible for neutrino events captured by in-ice detectors such as the Radio Neutrino Observatory in Greenland (RNO-G). The more prominent Askaryan effect is the consequence of interactions differing between shower particles with the surrounding medium, leading to negative charge access on the shower front and a positive charge access along the shower axis [4]. RNO-G aims to capture these radio signals and analyse the arrival direction of the primary neutrino, from which natural particle accelerators in our universe can be identified. Because of the small cross-section of neutrinos, the medium in which they are supposed to interact is required to be very large to maximise the chance of detecting them, and additionally has to be transparent to the radio waves emitted. For this, multiple stations with radio antennas are built in a grid with a 1.25 km spacing at a depth of up to 100 m (328.1 ft) in the ice [4]. Not only are these stations very far apart, but also at a very remote location, near the summit of Greenland at 3210 m (10 530 ft) above the sea level [5]. This means a central power distribution system is not feasible, and each station needs to produce energy for itself. To achieve this, two 120 W solar panels, each 8275 cm^2 (1283 in^2) in size, and a horizontal axis wind turbine with a diameter of 50.4 cm (40 in), produce power for the station while charging four deep cycle gel batteries to create a buffer for cloudy periods, windless times and the night. While the solar panels deliver more than enough energy during summer times, ideally the wind turbine should take over in the winter (October - March) when the sun does not rise above the horizon. Looking at

previous experiments detecting cosmic neutrinos, it is quite clear that further increasing the sensitivity in the ultra-high neutrino energy region ($E_\nu \gtrsim 10\,\mathrm{PeV}$) is important to understand astrophysical processes and discover new physics. Even though the IceCube project achieved the goal of detecting neutrino flux in part of the high neutrino energy region ($20\,\mathrm{GeV} \lesssim E_\nu \lesssim 10\,\mathrm{PeV}$) and even identified some sources, it was only possible to put a limit on the neutrino flux in the UHE region. The collaboration around RNO-G not only seeks to improve on that limit, but also to detect the actual flux of neutrinos. To achieve this goal, the sensitivity to neutrinos must be maximised, while the experiment must run for as long as achievable. As the detector is currently inoperable every winter due to the absence of sunlight, the run time could be almost doubled if the wind turbine generated enough power to satisfy the station's energy requirements. Thus, the stations should operate on as little power as possible, while the turbine must deliver power regularly in order to charge the batteries. Simultaneously, reducing the background noise increases the trigger sensitivity. Reducing and accounting for unwanted signals is indispensable to achieving the desired precision. The frequent high wind speeds on the flat glacier ice are both extremely beneficial for generating power, but can also supposedly negatively influence noise signals through the triboelectric effect. The goal of this work is to provide a deeper look at the power generation of the turbines in the field, determine their usefulness and shortcomings, and inspect the trigger rate of the stations in relation to wind velocity and acoustic background noise. Data on the power delivered by the turbines are directly logged by the RNO-G collaboration. The wind speed readings are taken by the National Oceanic and Atmospheric Administration (NOAA) at Summit station [6], which are freely available on the given website. The background noise produced by the wind is recorded with a hydrophone buried in the ice on site (station 13) and compared to the fluctuations in the trigger rate.

2 Context

To provide a deeper understanding of the topic and establish familiarity with terminology, this chapter provides a brief description of neutrinos, their interaction, and detection as well as the RNO-G detector stations.

2.1 Radio Detection of Neutrinos

First of all, the basics of neutrino physics are important for understanding the detection principle and why the detector is built the way it is.

2.1.1 Neutrinos

Starting with the messenger particle itself, a neutrino (ν) is an elementary particle that is described by the standard model of particle physics. It is classified as a fermion, meaning it possesses a half-integer spin and is a member of the neutral-lepton subclass. Crucially, this means it does neither interact through the electro-magnetic force, as it is neutrally charged, nor through the strong force, as it's a lepton and not a quark - the other fermion subclass. Therefore, the only forces a neutrino interacts with are gravity and the weak force. As seen in Figure 1, neutrinos come in three different

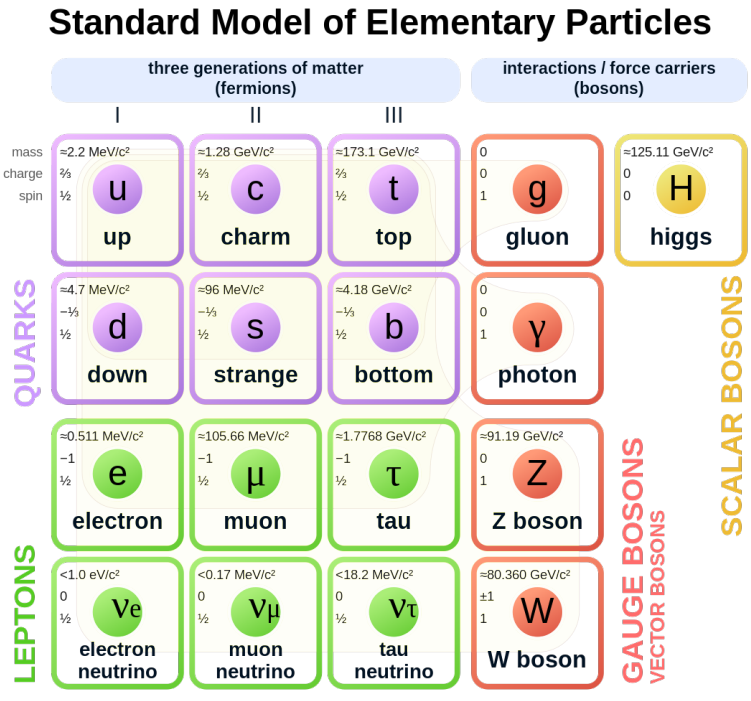

Figure 1: Particles of the Standard Model taken from [7]. The force-carrying particles (Gauge Bosons) are grouped in red. Leptons are marked in green, while quarks are shown in purple. The Higgs boson is the only member of its own scalar boson group in yellow.

flavours corresponding to the three charged leptons, the electron, muon, and tau-particle. This is especially important, since the events detected in neutrino detectors can differ depending on the flavour.

2.1.2 Secondary Particles

As previously stated, neutrinos cannot emit electromagnetic radiation, which would be the easiest signals to detect. Experiments with targeted energies above $\sim 20\,\mathrm{GeV}$ range need to rely on secondary particles created by neutrino-induced showers instead. Ultra-high energy neutrinos ($E_\nu \gtrsim 10\,\mathrm{PeV}$) scatter off a single quark in the nucleons inelastically, which disintegrates the nucleon, while what happens to the neutrino is subject to the specific type of interaction. Weak interactions can happen by exchanging either a neutral Z^0- or a charged $\mathrm{W}^\pm$-Boson. If the force-carrying particle is a Z^0-Boson, the interaction is called a neutral current (nc) and the outgoing particle remains a neutrino. Should the force-carrying particle be a $\mathrm{W}^\pm$-Boson instead, one speaks of a charged current interaction (cc). With a cc interaction between a neutrino and a nucleon, the outgoing particle will be a charged lepton corresponding to the flavour of the initial neutrino, as seen in Figure 2 [4]. The depicted deep inelastic scattering has the greatest interaction cross-section for interaction energies $E \gtrsim 20\,\mathrm{GeV}$ [8].

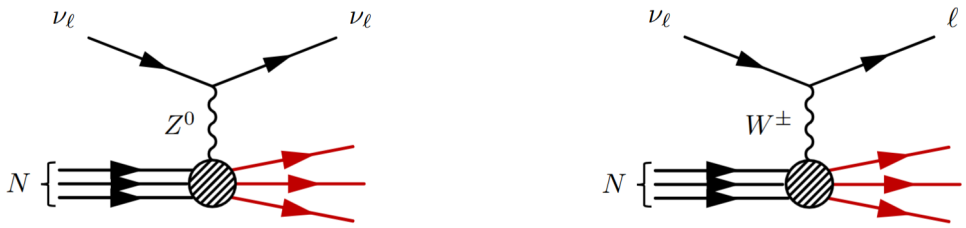

Figure 2: Deep inelastic scattering through the weak force between a neutrino and a nucleon. ν_l and l can be any pair of (ν_e, e^-), (ν_μ, μ^-), (ν_τ, τ^-). Left: Neutral current (nc) interaction with a Z^0-Boson. Right: Charged current (cc) interaction with a $\mathrm{W}^\pm$-Boson. Figures from [4]

From the destroyed nucleus, unstable pions are created, which decay after a short period of time, creating new particles in a cascade, until the energy contained within the particle shower is so diluted that no new particles can be produced. Figure 3 shows a schematic depiction of this shower.

2.1.3 Emission of Radio Signals

Two main mechanisms lead to the emission of radio signals in particle showers. In Ice, the dominant effect is the Askaryan effect. In comparison, the signals generated by the geomagnetic effect are negligible due to the short shower extension along the shower axis in ice [9]. The charge-excess effect (Askaryan effect) happens due to the ionisation of the medium the shower is propagating through. Negatively charged electrons are concentrated by and travel with the shower front, while the heavy, positively charged ions are left behind. Three different interactions lead to the acceleration of electrons in

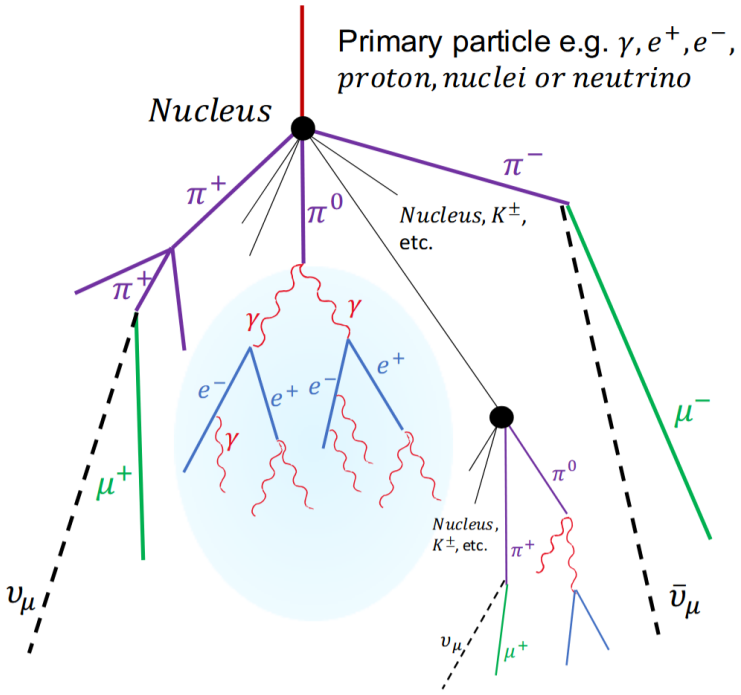

Figure 3: Simplified sketch of a particle shower. Green: muonic component. Blue: electromagnetic component. Purple: Hadronic component. Figure taken from [4]

the shower front [10].

$$\begin{aligned} \text{Møller scattering:} \quad & e^+ + e^- \rightarrow e^+ + e^- \\ \text{Bhabha scattering:} \quad & e^+ + e^-_{\text{medium}} \rightarrow e^+ + e^- \\ \text{Compton scattering:} \quad & \gamma + e^-_{\text{medium}} \rightarrow \gamma + e^- \end{aligned}$$

Electron-positron annihilation and Bhabha scattering slow shower positrons, adding to the charge separation [11].

$$\text{Electron-positron annihilation:} \quad e^+ + e^- \rightarrow \gamma + \gamma$$

This time-dependent charge $\dot{q}$ creates an electromagnetic pulse if the medium, in which the shower develops, is dielectric and non-absorptive [4].

2.2 RNO-G

After describing the principal RNO-G and other radio neutrino detectors work with, the specifics of the detector in Greenland can be discussed.

2.2.1 Detection of Radio Signals

Electromagnetic pulses produced through the Askaryan effect are measured with antenna arrays, consisting of Vpol- and Hpol antennas, at a depth of around 100 m. As their

names suggest, the two types of antennas are built to detect vertically and horizontally polarized radio signals, respectively. Additionally, three groups of three LPDA (**L**og-**P**eriodic **D**ipole **A**rray) antennas in different orientations on the surface help with detecting signals and reducing noise signals arriving from above the ice surface [4].

2.2.2 Sensitivity of RNO-G

Measuring the tiny electric field oscillations in the order of $\sim \frac{\mu V}{m}$ of the radio signals, and subsequently reconstructing from which direction the original cosmic ray arrived, requires an immense amount of precision. To achieve the outlined sensitivity in Figure 6, background noise must be kept to a minimum, while an extended up-time contributes very positively to it as well; two aspects which will be further discussed in this work.

2.2.3 Station Characterization

In this section, the technical assembly of an RNO-G station is described, starting with the power delivery system. As one can see in Figure 7, every station is equipped with a WT10 turbine, producing up to 500 W and two 120 W solar panels. Most recently, the solar panels are upgraded to deliver a combined wattage of 350 W. Some specifications of the older panels are listed in Table 1. At the same time, the turbine's performance characteristics are an essential part of this work and will be discussed in detail in section 3.2.

	RNO-G solar panels	
Power	120 W(×2)	180 W(×2)
Nominal Voltage	24 V	24 V
Module Efficiency	14.6 %	17.8 %
Dimensions	122.3 cm × 67.4 cm	150.4 cm × 67.4 cm
Area	8051.5 cm^2	10 137.0 cm^2

Table 1: Most relevant specifications of the solar panels, which the RNO-G stations are equipped with. The data sheets can be found in [13] and [14] for the 120 W and the 180 W panel, respectively.

Moving along the chain, the power input is fed through Electromagnetic Interference (EMI) filters to the charge controller in an insulated enclosure - a pelican case, used to protect the electronics from the cold and humidity. The electronics inside are presented in the schematic at the bottom of Figure 8. Energy from the turbine and the solar panel, which is not used to power the station right away, is stored in four 97.6 Ah@20°C (20 h-rate), or equivalently, 108 Ah (100 h-rate) deep cycle, lead acid batteries. These 12 V batteries are connected to pairs in a series configuration to achieve a system voltage of 24 V. The two pairs are connected in parallel afterwards, in order to maximize storage capacity of approximately 5 kWh at room temperature. Due to the extreme cold, this value is decreased drastically, which will be a point of discussion in Section 3.2. Even though the battery bank is shown to be within the pelican case in Figure 8, in newer revisions, the energy storage system (batteries and power box) is placed into a separate enclosure as seen in Figure 12. This is soon to be reverted to a single enclosure design

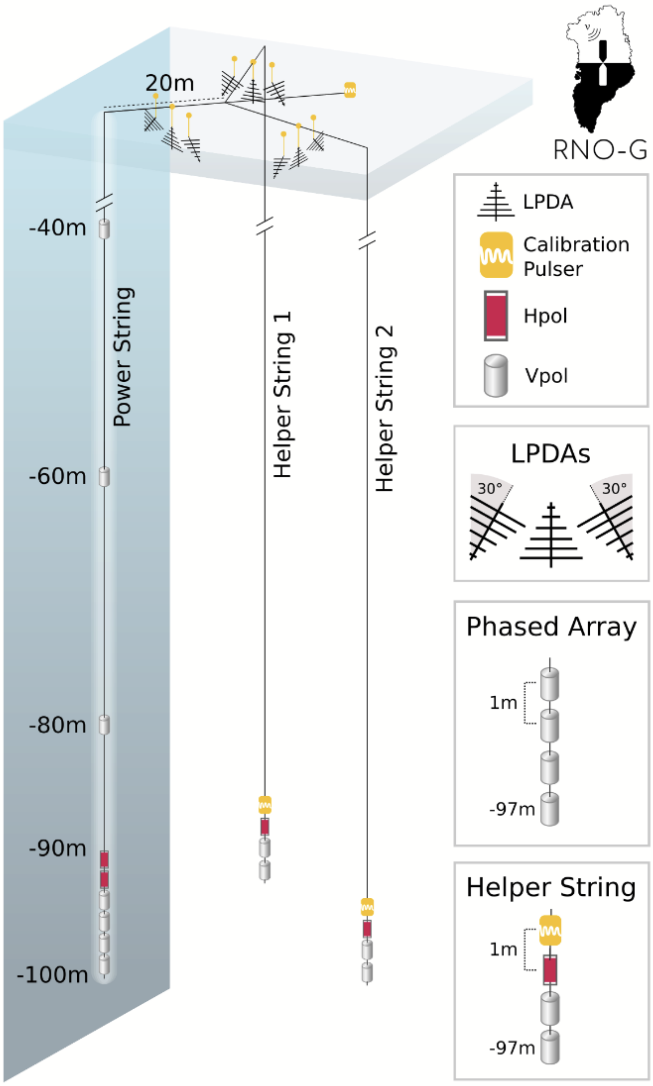

Figure 4: Schematic layout of the detectors of a single RNO-G station. Nine LPDAs are arranged on top of the ice sheet while 3 strings with V- and Hpol antennas are lowered into pre-drilled holes. The single phased array on the power string is responsible for triggering on neutrino events. Figure from [4]

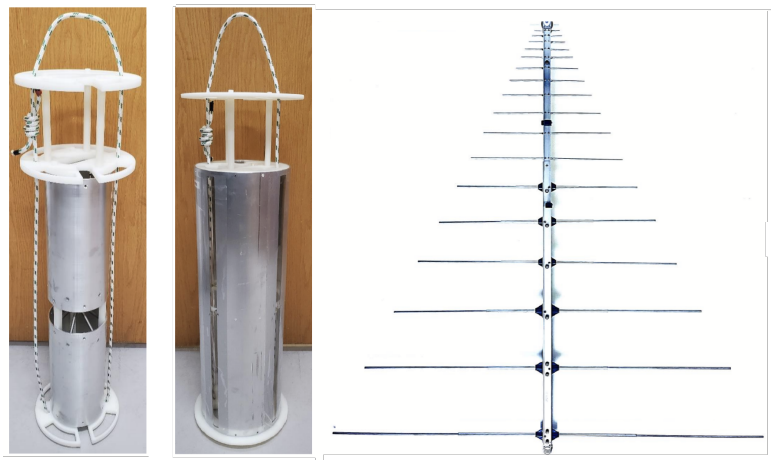

Figure 5: The different types of antennas used in RNO-G's stations are from left to right: Vpol, Hpol, and LPDAs. Pictures are taken from [12].

in future station upgrades, as otherwise the temperature of the batteries is too low.

The RADIANT (**RA**dio **DI**gitizer and **A**uxiliary **N**eutrino **T**rigger), FLOWER (**FL**exible **O**ctal **W**av**E**form **R**ecorder), amplifiers, and the calibration pulsers (both on the surface and in the bore holes) receive power directly from the power regulation and distribution system on the controller board, which concludes the power chain.

The signal chain begins at the previously mentioned LPDA, Vpol, and Hpol antennas. The LPDAs on top of the ice sheet are connected to the surface amplifiers, while signals from the V- and Hpols are fed to the downhole amplifiers. Images of the different antennas are shown in Figure 5. The amplified RF signal is sent to and processed by the RADIANT and the FLOWER, from which the digital data is moved to the controller board and stored on an SD card. To access the station and transfer files, wireless communication is achieved through an LTE (**L**ong-**T**erm **E**volution - a telecomunication standard) modem or a LoRaWAN (**Lo**ng **Ra**nge **W**ide **A**rea **N**etwork) transceiver.

2.2.4 History of Wind Energy at RNO-G

That the stations would need to rely on wind energy for about half of the year had been clear early in the planning of the detector. In 2022, two stations (11 and 12) were equipped with tandem Savant Turbines; tandem meaning two turbines were attached to either side of a pole. These were inspired by the design used at the ARIANNA detector [15]. Turbines of the Savant design consist of two vertical blades with a semi-circular shape, which twist from top to bottom as they spiral around each other. An example can be seen in Figure 9.

However, these turbines were very prone to freezing. In 2024, the turbines at stations 11 and 12 were replaced with the WT10 turbines shown in Figure 7. Additionally, the new stations 13, 14, and 23 were also equipped with one. Unfortunately, the problem of frozen turbines persists as Figure 7 demonstrates. Many possible fixes have been proposed, including coating the turbine and its blades with Teflon or special paint, replacing the lubricant with one better suited to extreme cold, or even turning the

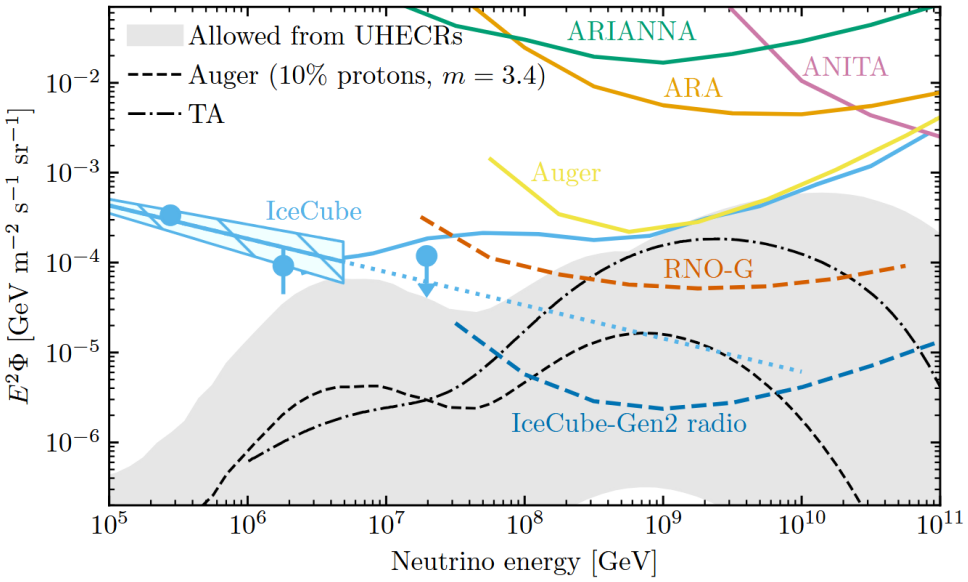

Figure 6: All colored lines represent the 90% confidence levels for the upper sensitivity limit of each experiment mentioned. IceCube's diffuse neutrino flux and upper limit represent the best current measurement in this energy region. RNO-G is predicted to increase the sensitivity, where IceCube could not see the neutrino flux. Figure taken from [8].

generator of the turbine into a motor to use a bit of power to initialise the spinning.

In the summer of 2025, the larger WT14 turbine, which is still in development, was installed at station 12. Its longer blades could provide extra torque to break the ice more easily. However, data on this has not yet been recorded.

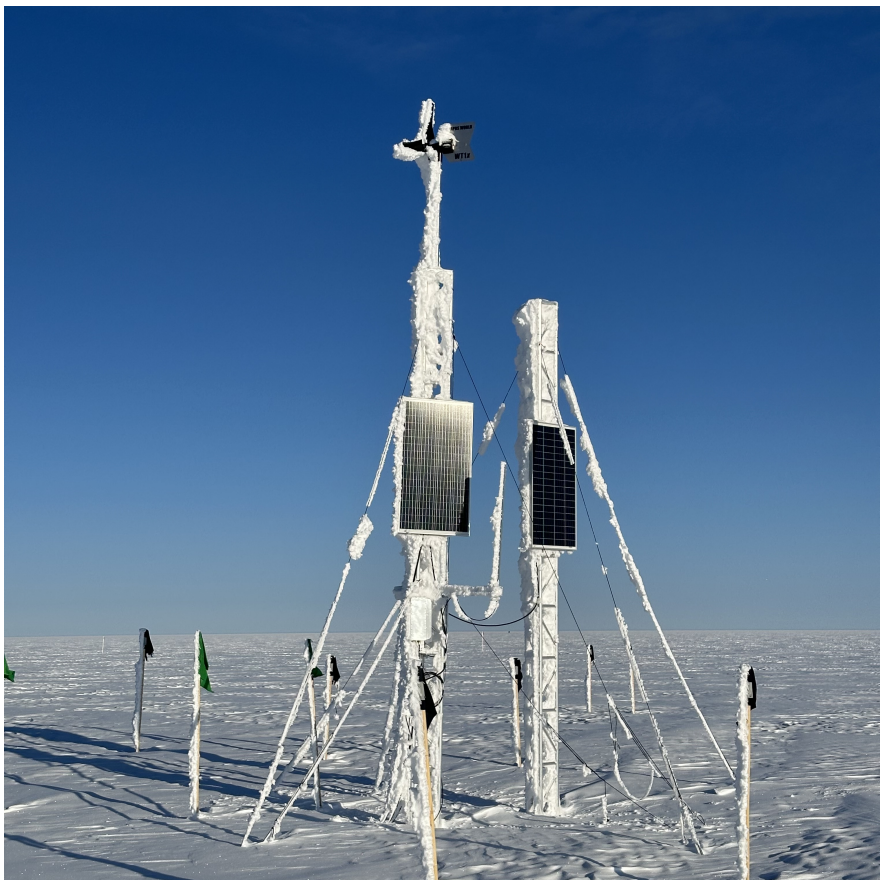

Figure 7: The picture shows the frozen-over power delivery system of station 13. A WT10 turbine sits upon the left service tower, while both towers are equipped with a 120 W solar panel.

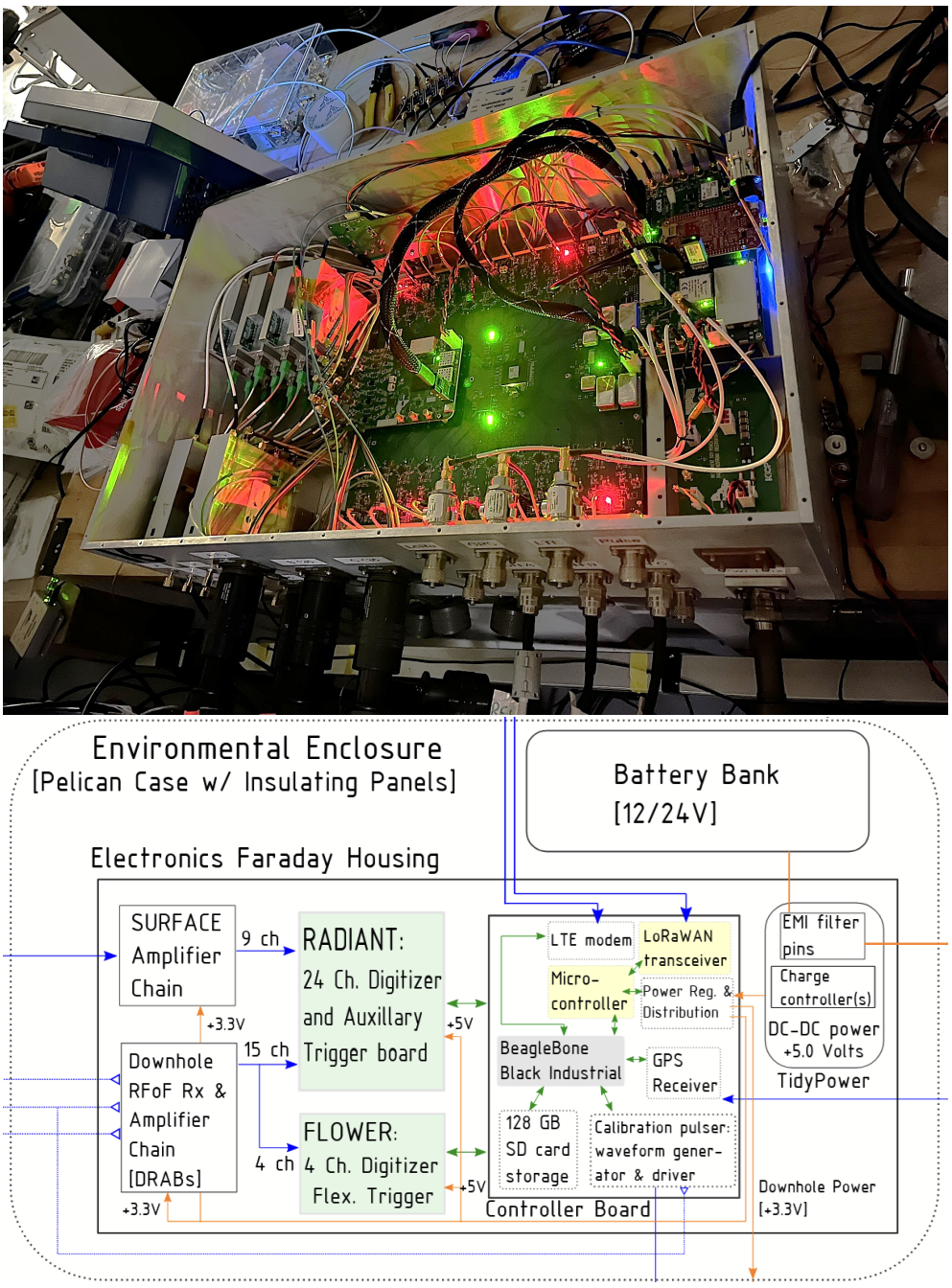

Figure 8: The "Electronics Faraday Housing" from the bottom Figure shows what is included in the instrument box from the figure on top. The layout is mostly accurate; however, due to its high utility, the controller needed to be illustrated larger than it actually is. It is located in the top-right corner of the upper figure. In later revisions, the battery bank and power box are packaged into a separate insulated enclosure at the moment. An example can be seen in Figure 12. This is soon to be reverted to a single enclosure design in future station upgrades.

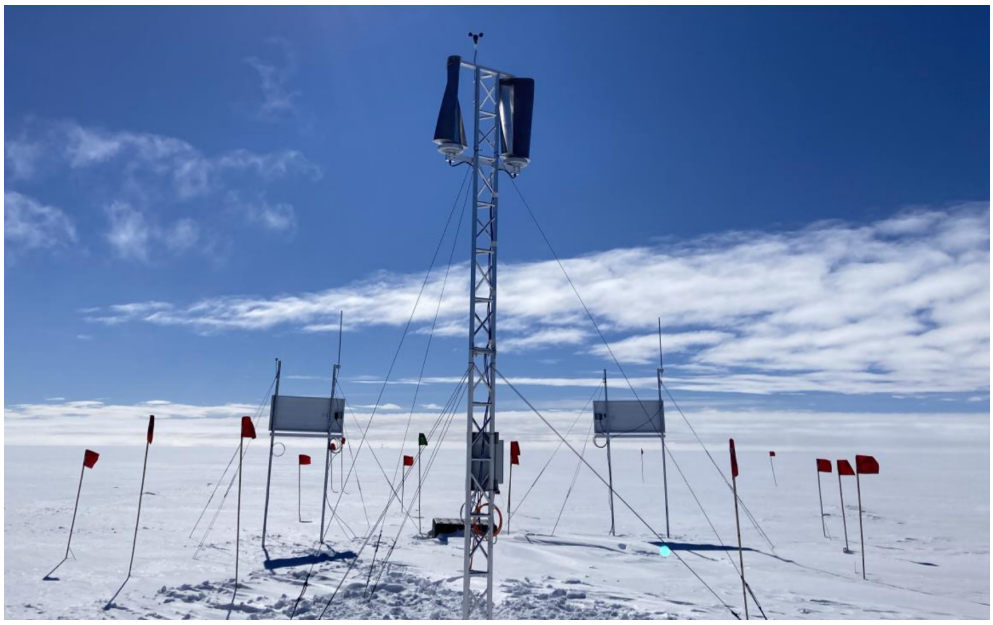

Figure 9: Tandem Savant Turbine at station 12.

3 Wind Power Performance

Extracting wind energy to power the stations is an essential goal of the RNO-G collaboration. Even though many solutions have been proposed and tested, including different types, sizes, and quantities of wind turbines, the power generation remains insufficient to this day. Evaluating the current wind power data is essential in finding the current shortcomings. In addition, a local setup of the power system is built at the **E**rlangen **C**entre for **A**stroparticle **P**hysics (ECAP). This not only provides the opportunity to compare the performance of the turbine under calmer conditions but also serves to facilitate the testing of new firmware and hardware without compromising one or more stations used for actual neutrino detection.

3.1 Local Experimental Setup

The power station utilizes as many parts as possible sourced directly from the RNO-G project. However, due to delivery restrictions and budgeting constraints, some parts differ from the actual components used in RNO-G detector stations; these are replaced by parts with specifications similar to the equipment in the field. An overview of the setup can be found in Figure 10. The individual parts and their functions are described in section 3.1.1, followed by the building process in section 3.1.2.

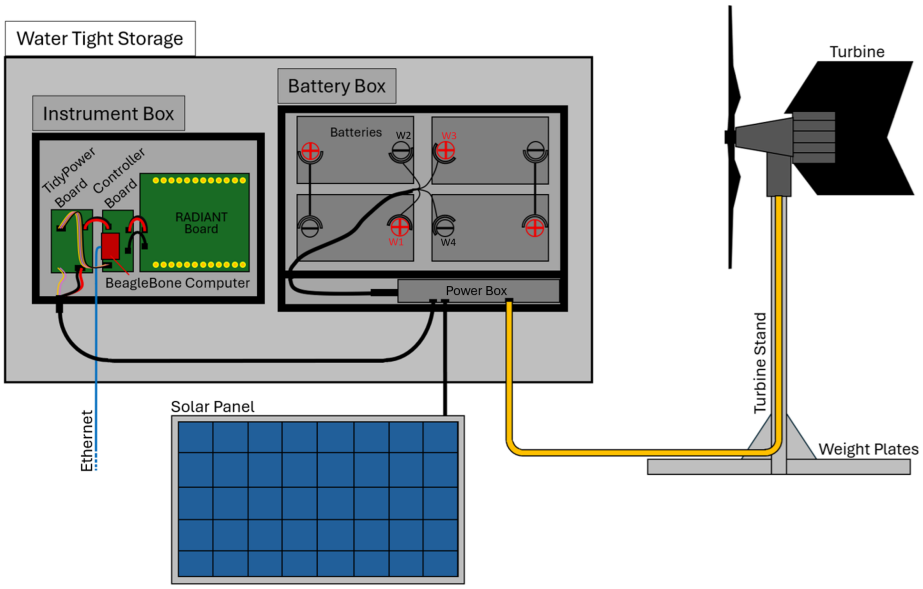

Figure 10: Schematic of the RNO-G Power Station at the ECAP building. The main components are labelled.

3.1.1 Hardware

The instrument box (see Figure 11) houses the RADIANT board, which is normally connected to the 24 antennas (Vpol, Hpol, and LPDA) and is controlled by the aptly named controller board. This all-in-one, Linux-based Beaglebone computer supports

communication over the SSH networking protocol either locally through USB or remotely via the connected Local Area Network (LAN). Located next to these two devices is the "tidy-power-board" designed by RNO-G itself. It handles cleaning of the input power for the RADIANT and the controller, as well as translating the I^2C bus signals.

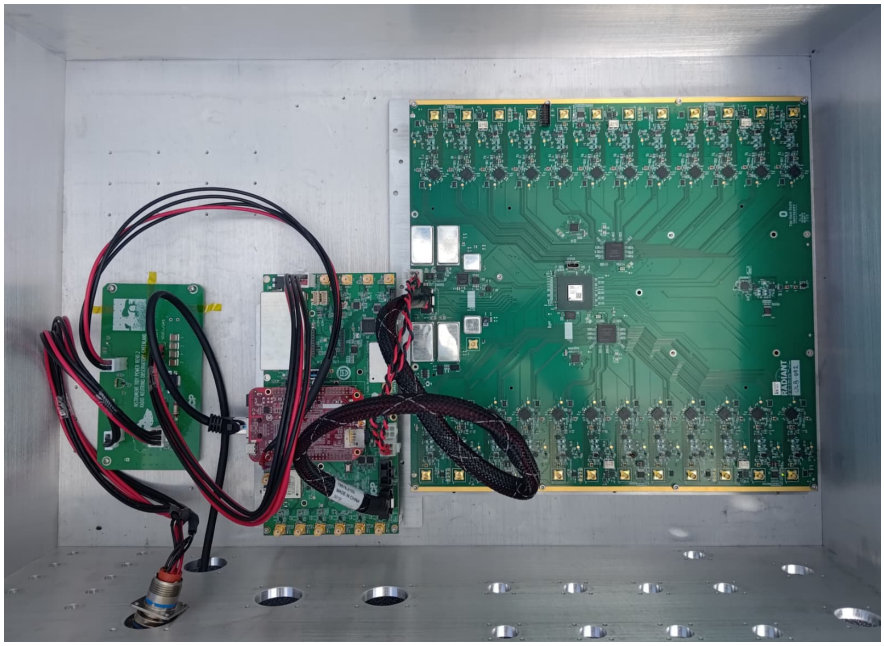

Figure 11: Displayed are the insides of the instrument box. From left to right, the circuit boards are the "tidy-power" board, the controller board (Beaglebone computer in red), and the 24-channel RADIANT board.

Shown in Figure 12 are the four deep cycle lead-acid batteries, each with a nominal capacity of 96.7 Ah@20°C(20 h-rate), that power the station. This differs only slightly from the 97.6 Ah-batteries used in the RNO-G stations. The power input of the turbine and the solar panel, as well as the charging of the batteries and discharging to divert load, is handled by the power box in front of the batteries (see Figure 12), which is also custom-built by the RNO-G project. The different connectors of the power box can be seen in Figure 13.

To keep the batteries charged, a 100 W polycrystalline solar panel is placed next to the station. Even though RNO-G stations are equipped with two 120 W solar panels, the local station not only does not have to power any data-taking components for radio signals, but the sunlight is also more intense at Erlangen compared to Greenland's summit location.

This means a single solar panel suffices. Some key attributes of the solar panel in comparison to one of the solar panel types used with RNO-G stations are noted in table 2, both of which are taken from their respective data sheets. A picture of the ECAP solar panel is displayed in Figure 14.

Also contributing to the power budget is a three-spoke horizontal-axis wind turbine with a diameter of 100.8 cm.

This turbine is the exact model used with the RNO-G stations and is rated for wind

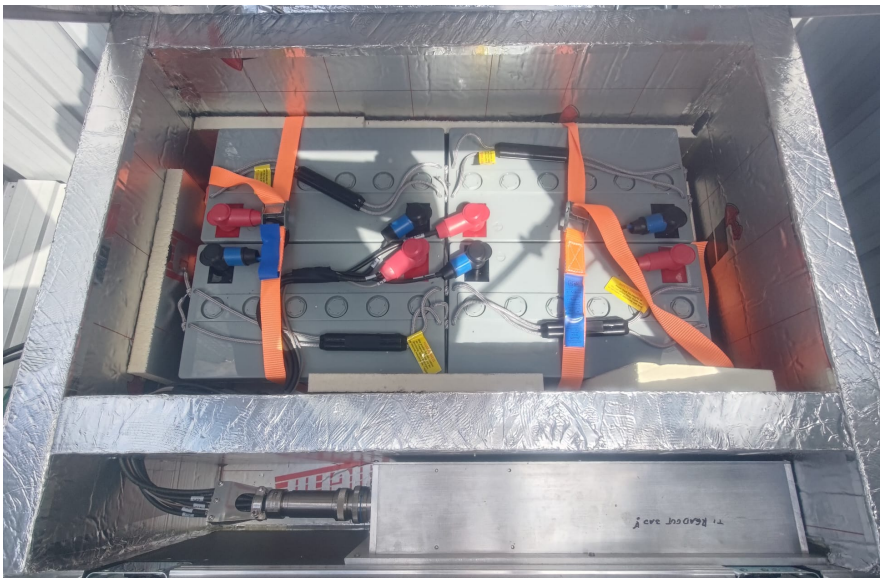

Figure 12: Insides of the battery box. In the back are four 96.7 Ah deep-cycle gel batteries. Two batteries are each connected in series, and both pairs are joined together in a parallel configuration. The four batteries are internally connected to the power box in the front.

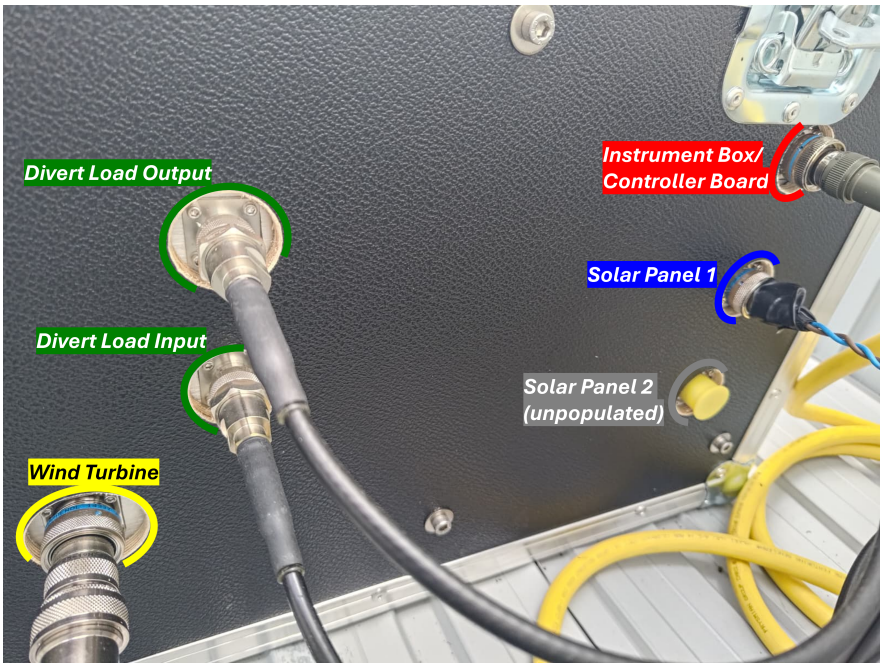

Figure 13: External connectors of the power box are fed through the battery box and connected to various devices, either generating or consuming electricity.

Figure 14: 100 W polycrystalline solar panel placed on the ground of the roof in front of the station.

	RNO-G solar panel	ECAP solar panel
Power	120 W(×2)	100 W
Nominal Voltage	24 V	24 V
Module Efficiency	14.6 %	13.6 %
Dimensions	122.3 cm × 67.4 cm	100.1 cm × 73.4 cm
Area	8051.5 cm^2	7347.3 cm^2

Table 2: Most important specifications of ECAP solar panel [16] compared to one of the solar power system of an RNO-G detector station [13].

speeds up to 70 $\frac{m}{s}$ while the generator can produce up to 1 kW of power. According to the manufacturer's specifications, it is supposed to start turning at 4.5 $\frac{m}{s}$.

Similar to the RNO-G stations, the turbine is mounted to a pole. The towers in Greenland are dug into the ice to provide stability under high winds. Since this is not an option for the local station, a different solution is required. The pole is supported by stone plates surrounding it, acting as a counterweight and also lowering the centre of gravity.

To calculate the mass required to prevent the turbine stand from tilting over, three factors must be considered. First of which is the force on the turbine depending on wind velocity. This formula is provided by the manufacturer [17].

$$F_{\mathrm{x,max}} = 0.255 \, \frac{\mathrm{kg}}{\mathrm{m}} \cdot v^2 \tag{1}$$

The second factor is the local maximum wind speed. The city of Erlangen has records of the highest measured wind velocities since 1991, of which the highest speed will

Figure 15: Horizontal-axis wind turbine installed on the roof of the ECAP. At present, the hub height of the turbine is 160 cm and is to be increased in future improvements up to 300 cm. The weight plates are already specced for the future height.

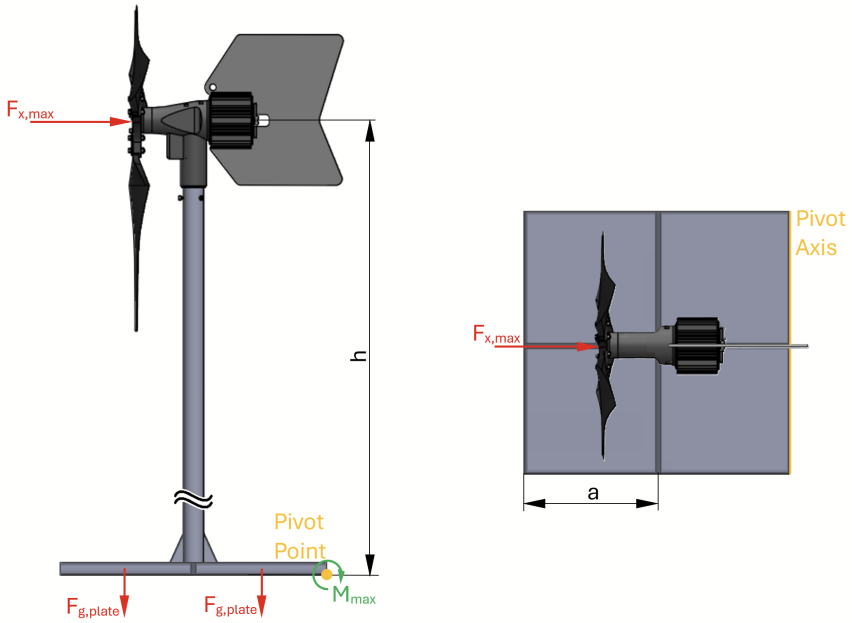

Figure 16: Schematic of the turbine setup at Erlangen. The technical drawing of the manufacturer [17] is edited to fit the needs of the mounting solution on the roof.

be regarded as the maximum [18]. The ECAP possesses wind records itself; However, the maximum wind speed is lower than the maximum of the city's records. For safety reasons, the highest possible value, i.e., the maximum of the city's measurements (20.11.2015), is used in the calculations.

$$v_{\max} = 34.5\,\frac{\mathrm{m}}{\mathrm{s}} \tag{2}$$

The maximum force on the turbine can thus be determined to be

$$F_{\mathrm{x,max}} = 0.255\,\frac{\mathrm{kg}}{\mathrm{m}} \cdot \left(34.5\,\frac{\mathrm{m}}{\mathrm{s}}\right)^2 = 303.51\,\mathrm{N} \tag{3}$$

Thirdly, the height of the turbine plays a significant role in how much torque the post needs to withstand. Additionally, the height is constrained by the protective volume of the lightning rods covering the roof. To calculate the torque on the base of the stand, a simple schematic (Figure 16) can be drawn.

$$\begin{aligned} M_{\max} &= F_{\max} \cdot h && (4)\\ &\leq M_{\mathrm{weight}} && (5)\\ &= 4m_{\mathrm{plate}} \cdot g \cdot a && (6) \end{aligned}$$

Here M denotes torque, h is the hub height of the turbine, m is the mass of the counterweight plates, $g = 9.81\,\frac{\mathrm{m}}{\mathrm{s}}$ is the local gravitational constant, and a is the side length of a single weight plate. With a maximum hub height of 3 m, the maximum torque and therefore the required side length of the plates can be determined.

$$M_{\max} = F_{\mathrm{x,max}} \cdot h = 303.51\,\mathrm{N} \cdot 3\,\mathrm{m} = 910.54\,\mathrm{Nm} \tag{7}$$

As Figure 17 shows, every combination in the yellow region above the red line is sufficient to stabilise the turbine stand. Eight plates with a side length of 50 cm and a total mass of 230 kg are enough to protect the turbine post from tilting over even under the highest winds. To make sure the turbine perfectly fits into the pole, an adapter piece is manufactured with the exact dimensions of the turbine and the stand. Also attached to the turbine pole is the divert load (designed by RNO-G), which displaces superfluous energy as heat if the batteries are fully charged (Figure 18).

3.1.2 Assembly

Instrument Box The instrument box is manufactured from aluminium plates in Chicago and assembled with 92 4-40 stainless steel Phillips head screws at a length of 11.18 mm (0.440 in). Both the RADIANT and the controller board are mounted to a separate mid plate with 4-40 aluminium spacers. Two cables, one for data and one for power, connect the two boards. Also connected to the Beaglebone on the controller board is the Ethernet cable, in order to control the station remotely. Six leads for power and two for the signal bus are connected to a MIL-spec socket (8-pin MIL-DTL-26482 12-8) with which the instrument box can be connected directly to the power box.

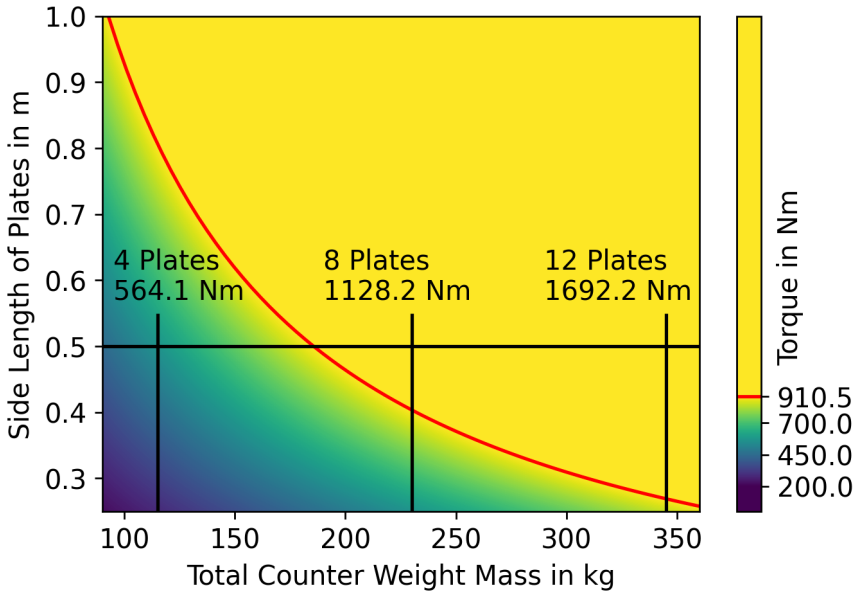

Figure 17: The contour plot shows the torque on the stand based on the counterweight and distance from the pole. For plates distributed around the pole as shown in Figure 16, the distance to the pole is the side length of a single plate. The red line marks the maximum torque the turbine would experience as calculated in equation 7. Marked in black are examples of 50 cm × 50 cm × 5 cm stone plates and how much counter torque they provide, calculated with equation 6. The plates used are sourced from a local hardware store and have a mass of 28.75 kg each.

Figure 18: The divert load used at the ECAP-Station. The same device is used at the RNO-G detector stations.

Battery Box Housed by the battery box are the four batteries and the power box. Before placing the batteries, the power box needs to be inserted into the front of the battery compartment. Due to an oversight while planning, a small slit has to be cut into the insulating foam to feed the connectors of the power box through the holes in the Battery box. After that, an intermediate layer of insulation foam is placed inside. A heating plate is mounted under the batteries to keep them from cooling down too far. This is especially important in cold environments such as Greenland, as Batteries lose capacity the colder they get. The manufacturer of the original batteries provides detailed information on how the batteries are affected, as shown in Figure 19.

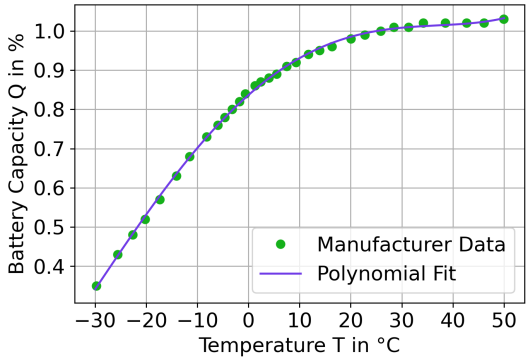

Figure 19: Capacity change depending on operating temperature of the gel battery used in RNO-G stations [19]. The data from the original graph is automatically digitized and fitted with a fourth-order polynomial.

Variable	Value	Error
a $\left[\frac{1}{°C^4}\right]$	3.1×10^{-8}	0.5×10^{-8}
b $\left[\frac{1}{°C^3}\right]$	-4.3×10^{-7}	2.2×10^{-7}
c $\left[\frac{1}{°C^2}\right]$	-2.08×10^{-4}	0.05×10^{-4}
d $\left[\frac{1}{°C}\right]$	1.15×10^{-2}	0.01×10^{-2}
e[1]	0.836	0.002

$$Q[\%] = a \cdot T^4 + b \cdot T^3 + c \cdot T^2 + d \cdot T + e$$

Table 3: Values for the polynomial fit shown in Figure 19.

Even though the temperature is of little concern for the ECAP station, the heating plate is installed regardless. The four batteries are lowered into the insulated box such that their terminals meet in the middle as shown in Figure 12. They are connected to pairs in series first, to achieve a system voltage of 24 V. One short cable for each battery pair connects the Ground (GND) from one to the high terminal of the other to complete the serialization. In order to minimize the risk of electrical shock, wearing rubberized gloves and safety glasses is advisable. After the bridges have been attached, the centre cluster can be mounted to the terminals. First, both GND terminals w2 and w4 are secured to the batteries, followed by w1 and w3. Connected to the power box are the aforementioned instrument box, the solar panel, as well as the wind turbine, and the divert load as seen in Figure 13. Solar Panel Mounted to an aluminium rail system, the solar panel is placed on the ground, weighed down by four 30 cm × 30 cm × 4 cm stone plates with an overall mass of $4 \times 7.7\,\text{kg} = 30.8\,\text{kg}$. The rail system allows for angling the solar panel towards the arch of the sun. Electrical connection is achieved by a specialized cable, which adapts the 3-pin MIL-DTL-26482 12-3 connector (one pin unused) at the power box to two standard MC4 connectors, most commonly used in solar plants. Wind Turbine The turbine is connected to the power distribution system with a four-lead cable and 4-pin MIL-DTL-26482 14-4 connectors on both ends. Three of the four leads carry voltage while the fourth one is used as ground in a typical 3-phase

setup. Before the turbine can be connected, the cable is fed through the stand, which the turbine will be mounted to afterwards. Secured with two bolts, the turbine can freely spin towards the wind direction.

Divert Load The divert load is attached to the turbine pole with two U-bolts as seen in Figure 18. Two coaxial cables can carry the current from the power box through the divert load and back. Any unused power that cannot be stored (i.e. if the batteries are already full) is diverted to this load, which relies on passive heat dissipation to get rid of any excess electrical energy.

3.1.3 Differences between the ECAP and RNO-G Stations

In this short section, the hardware differences between the test station at the ECAP and the detector stations from the RNO-G project are highlighted. The first difference is the absence of any antennas or radio data-taking components at the ECAP Station. While the ability to connect antennas to the station could be facilitated with the included RADIANT board, there are no amplifiers present to boost any kind of signal. This would be a bad idea in any case, as the radio background at the ECAP is way too loud for the highly sensitive instrument. Another component missing in the instrument box at the local station in Erlangen is the FLOWER, which is also only needed for measuring radio signals. All components, which are either missing or available at the ECAP test station are listed below with the differences of the power system specifications displayed in Table 4.

Components missing at the ECAP test station

- Radio Antennas (Vpol, Hpol, and LPDAs) and Calibration Pulsers
- LTE Antenna (Future upgrade)
- LoRaWAN Antenna
- GPS Antenna
- Surface and Downhole Amplifiers
- FLOWER

Components available at the ECAP test station

- Tidy-Power Board (from RNO-G)
- Controller board (from RNO-G) with BeagleBone Computer
- RADIANT (from RNO-G)
- Battery Pack
- Power Box (from RNO-G)
- WT10 Turbine
- Turbine Stand
- Solar Panel
- Divert Load (from RNO-G)

3.1.4 Future Improvements

Currently, the station does not operate at its maximum potential. The hub height of the turbine can be increased to the calculated maximum height of 3 m via an extension of the stand. This needs to be specially manufactured by FAU's local workshop and

	RNO-G	ECAP
Batteries	4× Deka Solar 8G31-HST 97.6 Ah@20°C(20 h-rate) [19]	4× CTM CTV 100 96.7 Ah@20°C(20 h-rate) [20]
Turbine	APRS WT10 Micro Wind Turbine [17]	
Stand	purpose built for in/on-Ice deployment	DUR-line Herkules 8PL XL 1.7 m [21]
Solar Panel	Ameresco 120JB-V [13] and Ameresco 180J-V [14]	Phaesun Sun Plus 100_24 [16]
	more details in tables 1 and 2.	
Divert load	Designed and manufactured by the RNO-G collaboration	

Table 4: Power system specifications of the RNO-G and ECAP test station.

was not ready to be built in time for the setup. For now, the turbine stands at a height of roughly 1.6 m.

The communication with the station is facilitated through an Ethernet connection to the local network. This means that, as long as one is able to connect to the ECAP network via Wi-Fi, LAN, or with a VPN, interfacing with the station is possible. However, this is only the case for ECAP employees due to regulatory access limitations. To lift this restriction, as well as to eliminate any and all wires, tethering it to the building, an LTE modem is to be installed in the future.

Another complication the station suffers from is an unsolved problem concerning the data transmission lines and bus signals. While the controller board and the connected RADIANT can be reached over the station's network connection without issue, the power data readout is hindered by package losses somewhere in the system. Due to the limited time available for this thesis, a full diagnosis was not completed. However, possible failure points are the soldered and crimped connections of the wires connecting the Tidy-Power board to the controller, as well as the power box, which already has an identified failure in the temperature sensor 1 readout. There needed to be modifications done to Tidy-Power board as well, which may have been improperly executed. Analysing the signal chain with an oscilloscope to identify where the signal degrades should clear up where the failure lies.

After clearing all faults, the local station will be used as a testing ground for hardware and software development. This ensures the full functionality of both the upgraded parts before rollout, as well as the detector itself during testing.

As the power data of the station at the ECAP cannot be read properly, the following analysis is limited to the real detector stations of RNO-G.

3.2 Power Data Analysis

The ultimate goal of this work is to compare wind power data from Greenland and Erlangen to identify irregularities arising from the extremely low temperatures at the detector stations, and to gain a better understanding of the power system's efficiency. Due to the technical issues previously mentioned, the data from Erlangen is not ready for the final evaluation. Therefore, only data from Greenland will be analysed. Since

this detector is still under construction, the data is very limited and only sporadically available. Figure 20 shows what is available for station 13. Due to the incomplete

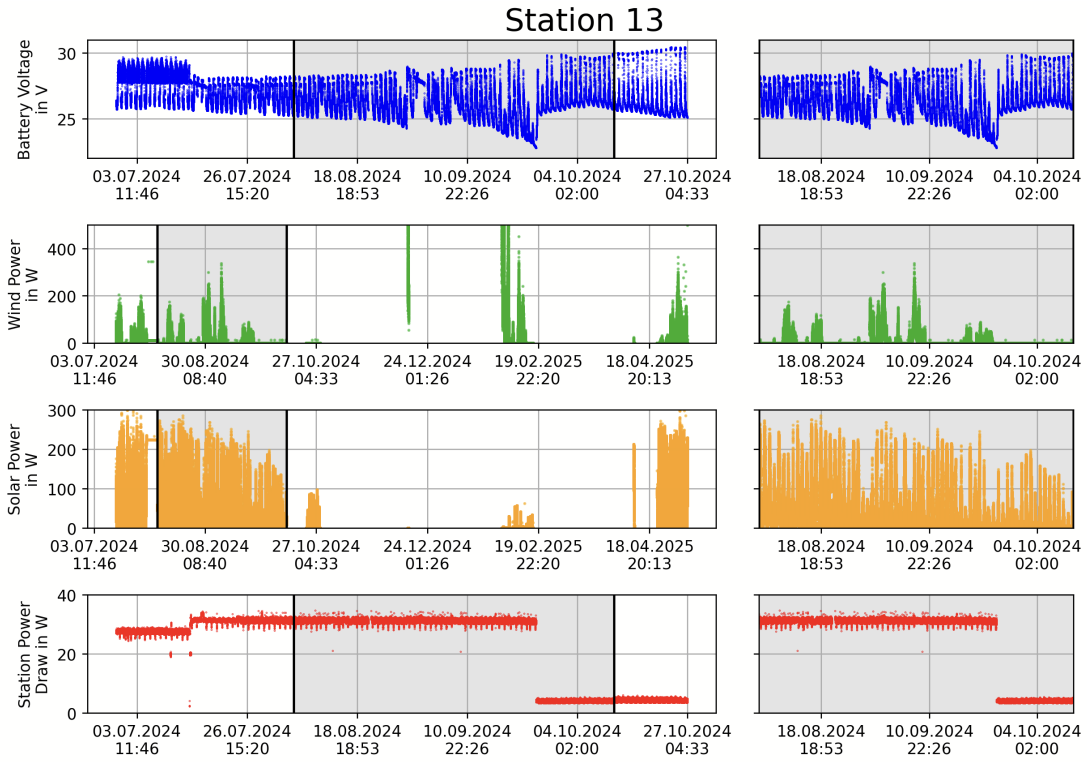

Figure 20: Overview of the available data for station 13. Generated solar and wind power, as well as the power draw of the station and the voltage of the battery pack, are displayed over time. The area marked in gray shows a time interval in which there is no interruption of the data of any variable and is shown in more detail on the right.

data, not all analysis steps are from the same time period. Depending on the objective, periods are chosen where the required data is available. For example, if a time period must be chosen where all data is recorded for station 13, it is possible from 05.08.2024 at 11:07:40 to 11.10.2024 at 19:10:48 (Figure 20, right side). However, should the assessment require fewer variables, more data is used. The station power draw in Figure 20 (red) already shows an interesting time period, where the station has switched from high to low power mode, indicated by the power draw changing from about 31.5 W to roughly 4 W.

For RNO-G, it is of utmost importance to have an efficient and reliable energy-generating system that harvests the high wind speeds. As alluded to in the introduction, the prolonged polar nights of several months necessitate the use of a renewable energy source other than photovoltaics. The first aspect of a functioning wind turbine is the onset wind speed, i.e., the necessary wind speed at which the turbine starts to turn. Since the turbine at the RNO-G station currently doesn't record its revolutions per minute (RPM), the turning will be equated to the power generated. The servers provide records of both the voltage and amperage of the turbines. Simply multiplying those values equates to the wind power shown in Figure 20 (green). The weather data is not

recorded for each RNO-G station individually, but at a single location at the Summit station. The weather data includes temperature, pressure, humidity/dew point, wind direction, wind- and gust speeds.

The following analysis uses station 13 as an example, while as much of the evaluation as possible is also conducted for the other operational stations, 11, 12, 14, and 23. The data from these stations is shown in the appendix (Section A.1).

3.2.1 Battery Voltage

The first examination of Station 13 focuses on the battery voltage level. As seen in Figure 20, the selected time frame is at a crucial point, where the available solar energy is dwindling due to the impending polar night. This means the battery is charged less every day, or in other words, the energy storage gets discharged more and more till the station needs to be switched into low power mode to conserve battery health. Interestingly enough, the maximum battery voltage rises simultaneously. This is attributed to the charge controller unit. Examining the temperature during the same time period reveals a clear downward trend (Top Figure 21). As the temperature around the batteries falls, so does their capacity. Information about the actual capacity loss is provided by the battery manufacturer, shown in Figure 19. To counteract this, the charge controller increases the maximum voltage. As the specification sheet describes this, the maximum voltage drops by $-0.060\,\frac{\mathrm{V}}{^\circ\mathrm{C}}$ for rising temperature [22]. This not only prevents undercharging in colder times but also protects against overheating and outgassing of the battery when it is warm [22]. For the linear fit in the bottom Figure of 21, the station temperature is divided into ten equal intervals. In each of these intervals, the corresponding maximum battery voltage is extracted and plotted. Even though the data is quite messy, especially with the temperature reading having a malfunction between July and August, the fitted function perfectly matches what is written in the data sheet, a voltage drop of $(-0.060 \pm 0.005)\,\frac{\mathrm{V}}{^\circ\mathrm{C}}$. As this only confirms what is already stated in the specification sheet, it will not be repeated for the remaining stations.

3.2.2 Wind Power and Efficiency

The second analysis is about the efficiency of the turbine. Wind tunnel tests under ideal conditions have already been performed by the RNO-G collaboration, to which this field data set will be compared. As shown in Figure 22, the output power and, more importantly, the efficiency curve of the wind turbine change depending on the test voltage. In the wind tunnel experiments, the test voltage simulates the battery voltage of the real stations, which changes depending on the charge state. A fuller battery corresponds to a higher battery voltage. To calculate the power efficiency coefficient of the wind power system, one has to divide the output power from the turbine by the available wind power [23]. The output power is the measured electrical power, so any efficiency losses from the generator are already included in the efficiency coefficient.

$$c_\mathrm{P} = \frac{P_\mathrm{out}}{P_\mathrm{available}} = \frac{P_\mathrm{out}}{0.5 \cdot \rho \cdot A \cdot v^3} \tag{8}$$

where ρ is the air density, A is the swept area of the rotor, and v is the wind velocity.

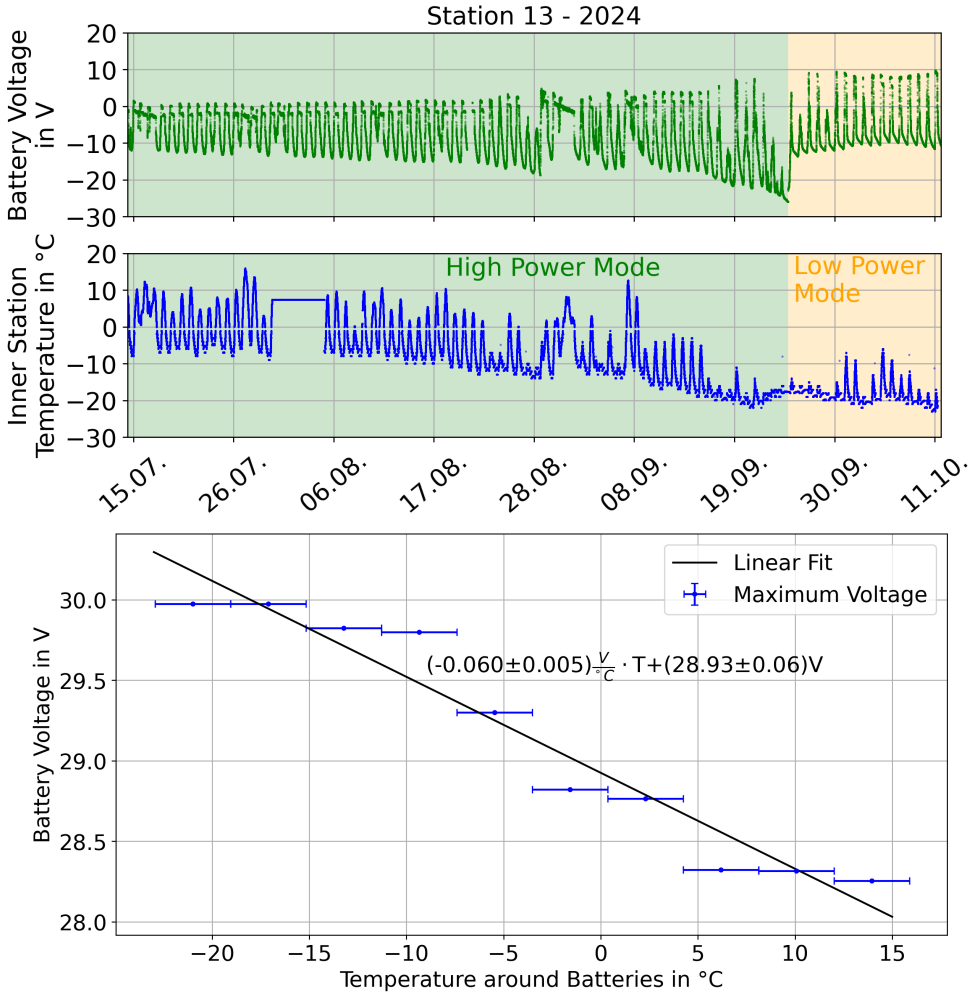

Figure 21: Top: Battery voltage and temperature of station 13 over time. Bottom: Maximum battery voltage over temperature with a linear fit.

For the wind tunnel test, it is assumed the experiment is performed at sea-level air pressure ($p = 101.32\,\text{kPa}$ [24]), as there are no records of the real-time pressure. There exists only one reading of the temperature, $T = 14\,°\text{C}$, and without a single humidity measurement, the air is presumed to be dry. From these two readings and the air's specific gas constant R_{Air}, the density during the wind tunnel test can be calculated by

$$R_{\text{Air}} = \frac{R}{m_{\text{mol}}} = \frac{8.314\,472\,\frac{\text{J}}{\text{mol}\cdot\text{K}}}{0.028\,965\,3\,\frac{\text{kg}}{\text{mol}}} = 287.049\,\frac{\text{J}}{\text{kg}\cdot\text{K}} \tag{9}$$

$$\rho_{\text{Lab}} = \frac{p[Pa]}{R_{\text{Air}}\cdot T[K]} = 1.229\,\frac{\text{kg}}{\text{m}^3}. \tag{10}$$

Air's molar mass as well as the value for the universal gas constant are taken from [25]. Since the environment of the field data consists of moist air, the calculation is slightly more complicated.

$$\rho_{\text{Field}} = \frac{p_{\text{partial}}}{R_{\text{Air}}\cdot T} + \frac{p_{\text{vapor}}}{R_{\text{vapor}}\cdot T} \tag{11}$$

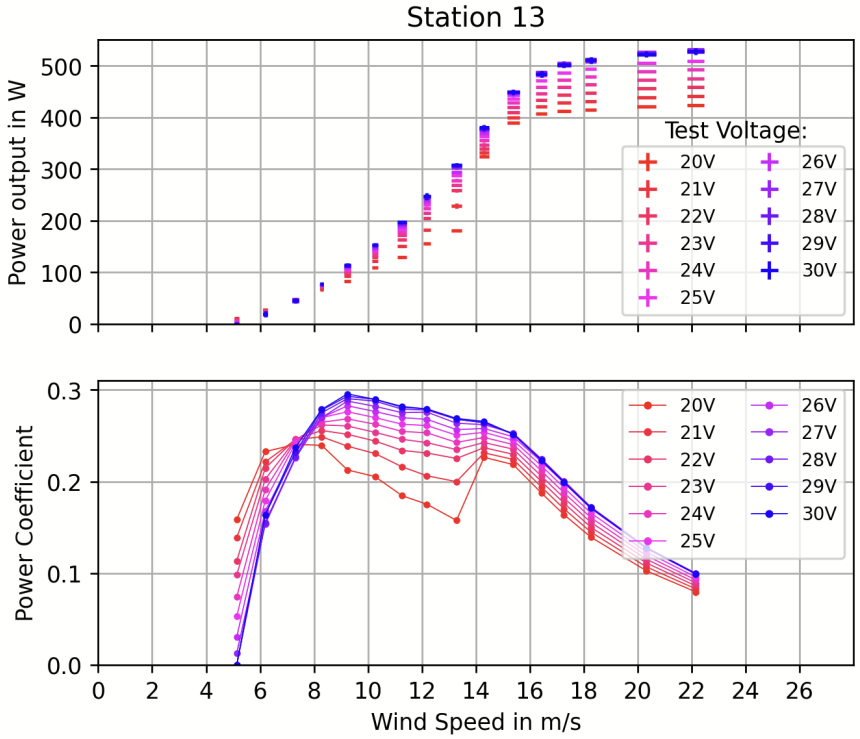

Figure 22: Top: Power output depending on the wind speed at a temperature of 14 °C of the WT10 turbine in a wind tunnel test. Bottom: Power coefficient as a function of wind speed, calculated from equation 8. The colors show the test voltage, which simulates the charge level of the batteries in the field.

Here, p_{partial} and p_{vapor} are the partial and water vapor pressure, which will be calculated shortly, while R_{vapor} is the specific gas constant for water vapor. The water vapor pressure can be computed by equations (6, Tetens' Formula) and (7b) of Richard Shelquist's article on air density and altitude calculations [26].

$$p_{\text{vapor}} = R_H \cdot C_0 \cdot 10^{\left(\frac{C_1 \cdot T[^\circ C]}{C_2 \cdot T[^\circ C]}\right)} \tag{12}$$

$$C_0 = 6.1078 \qquad C_1 = 7.5 \qquad C_2 = 237.3$$

R_H represents the relative humidity, which is included in the weather records and is, similar to the wind speed and pressure readings, averaged every minute. The partial pressure due to dry air is simply

$$p_{\text{partial}} = p - p_{\text{vapor}} \tag{13}$$

The air density in the field is processed for every point in time individually. It varies between 0.8302 $\frac{\text{kg}}{\text{m}^3}$ and 1.1272 $\frac{\text{kg}}{\text{m}^3}$. A full view of the air density data is shown in Figure 23.

To begin the field data analysis, it is essential to note that the voltage level of the batteries fluctuates constantly. Not only does it depend on the charge level, but the

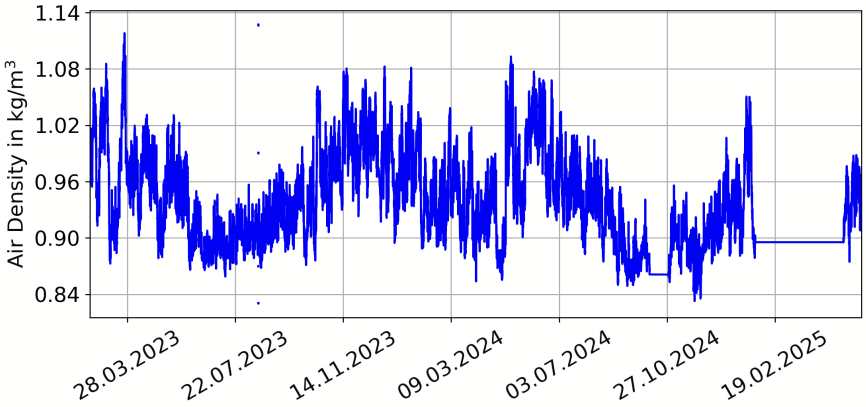

Figure 23: Air density calculated using equation 11 for the whole time range.

analysis at the beginning of this section also showed that the maximum voltage shifts depending on temperature. This means it cannot simply be separated from the power output, as was done with the wind tunnel data, which introduces a relatively big degree of uncertainty. However, it is still important to analyse the mean power and efficiency of the turbines. Since the power readings and the wind speed measurements are recorded by two different entities (RNO-G for station data, NOAA for weather data [6]), it makes sense that they are not updated simultaneously. The wind speeds are averaged over one minute, while the power readings are only measured every 20 s. To get a more precise result, the wind power is averaged over 5 minutes (15 data points) after the fact. To have these two sets work in conjunction with each other, the output power and velocities are subsequently linearly interpolated to a common timing. This allows for plots as in Figure 25.

Examining the bottom two plots in Figure 25 from left to right, the first significant detail is at the 6 - 8 $\frac{\text{m}}{\text{s}}$ mark. This is where the turbine begins to spin most of the time, which is close to the 4.5 $\frac{\text{m}}{\text{s}}$ the manufacturer specifies. This is best confirmed by the wind tunnel test, which shows an onset wind speed of 5 $\frac{\text{m}}{\text{s}}$ under ideal conditions. The next interesting interval is between 8 and 11 $\frac{\text{m}}{\text{s}}$. Here, the power output should be rising as it mostly does. However, there appear to be periods during which high wind speeds do not result in a higher power output. This can have multiple explanations. The easiest one is that the wind readings are not recorded at the same position where the power is generated. Nevertheless, this cannot be the single cause, as other wind speed intervals do not exhibit this extreme discrepancy. Another reason could be icing on the turbine, preventing it from spinning. This can explain the structure, as below 8 $\frac{\text{m}}{\text{s}}$ there is less power generation anyway, and higher wind speeds $> 11 \frac{\text{m}}{\text{s}}$ could help break free the turbine. In reality, it is probably a combination of the above and more. These time periods can be manually excluded from the data set to see how they affect the power output and efficiency curve. One such time period is displayed in Figure 26 with the resulting power output and power coefficient in Figure 27. One can clearly see that the median of the data without the cut periods follows the wind tunnel data more closely in the beginning and exhibits smaller deviations from the median in the 16th and 84th percentiles. The displayed example of a cut time period shows the power output of the turbine, as well as the wind speed data and the calculated theoretical output power.

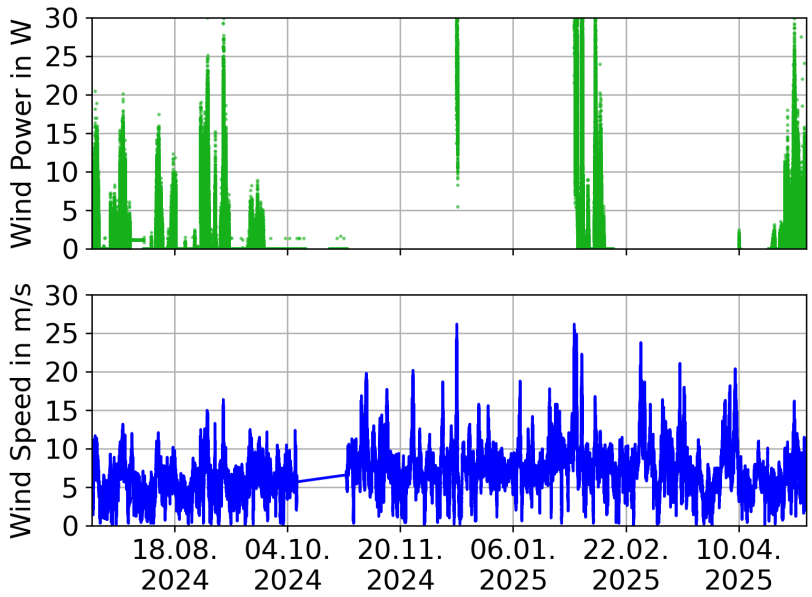

Figure 24: Wind power delivered by the WT10 turbine on station 13 (top) and available wind speed data from Summit station at the time (bottom). The wind speed is measured every 60 s while the station's power readings are updated every 20 s

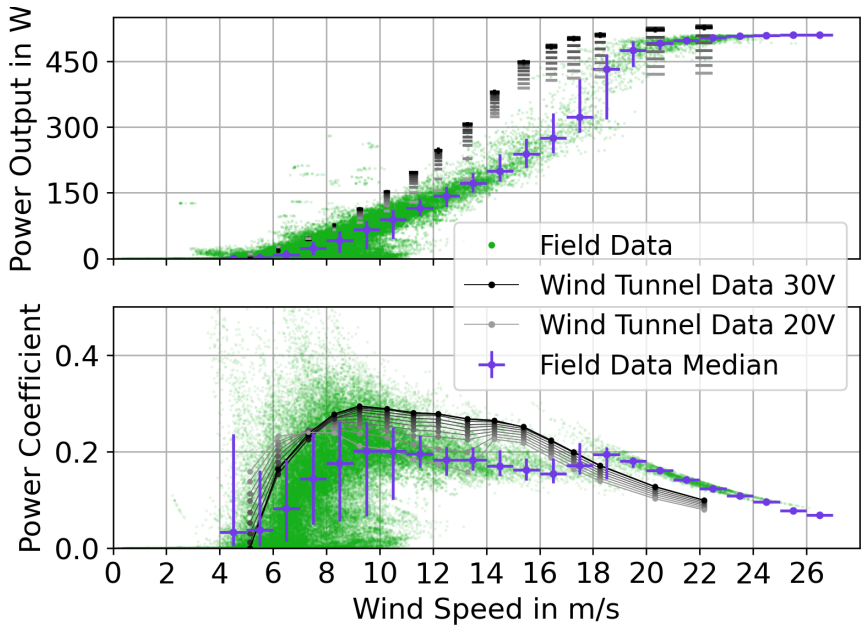

Figure 25: Top: Power output of the turbine. Bottom: Power efficiency coefficient of the turbine depending on wind speed. Both plots feature the raw data and the median, with the 16th and 84th percentiles. The expected values from the wind tunnel test are included as well. The power coefficient is calculated as described in equation 8. The power data is averaged across 5 minutes (15 data points) to achieve a more precise measurement.

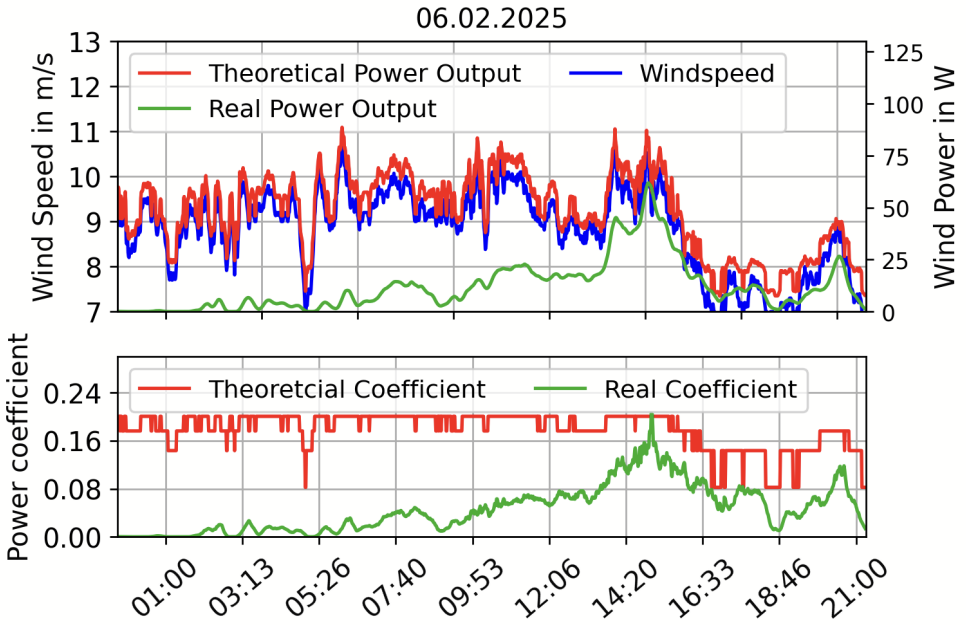

Figure 26: Top: Wind speed together with both the real and theoretical power output of the turbine. Bottom: Real and median power coefficient for the given wind speed and power output on the top.

The theoretical output power per wind velocity is calculated by computing the available input power and multiplying by the corresponding median power coefficient seen in Figure 25.

$$P_{\text{theoretical}}(v) = c_{\text{P}}^{\text{Median}} \cdot P_{\text{available}}(v) \tag{14}$$

$$= c_{\text{P}}^{\text{Median}}(v) \cdot 0.5 \cdot \rho \cdot A \cdot v^3 \tag{15}$$

The data from February 2 is especially interesting as the power output of the turbine is fairly inconsistent throughout the day, even though the wind speed does not vary as much. When comparing the theoretical power output to the actual one, the turbine consistently underdelivers throughout the day, but the early hours are particularly poor. While this kind of data is incredibly interesting for discovering the hindrances of the wind power system, precisely identifying the problems is beyond the scope of this work. The cuts are applied only rudimentarily. Therefore, a more sophisticated scientific method would need to be developed to identify and isolate these regions in order to analyse inefficient performance in the future. All further analysis in this work will focus on the uncut data.

With that being said, underperformance is not the only issue in the sub 11 $\frac{\text{m}}{\text{s}}$ region. The power coefficient also shows a significant over performance between 6 and 10 $\frac{\text{m}}{\text{s}}$. This is likely a consequence of outliers in the data, which are accentuated by the averaging and interpolation step. To reduce this issue in the future, the pure data should be cleaned of those outliers before averaging.

The next important feature is again a significantly lower power output by the turbine. Starting from 10 $\frac{\text{m}}{\text{s}}$ up to 18 $\frac{\text{m}}{\text{s}}$, the power output dips very low under the wind tunnel

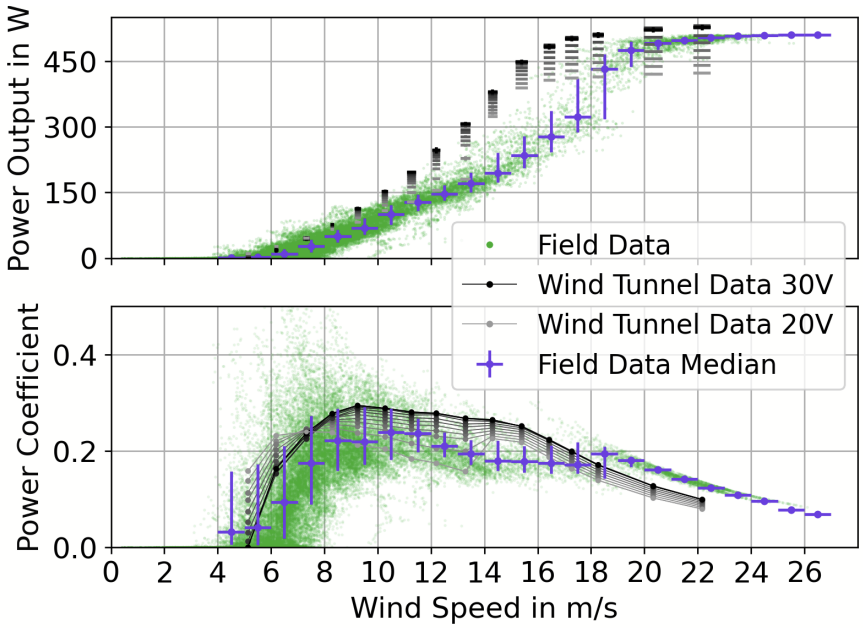

Figure 27: Shown are the same plots as in Figure 25 of station 13, but with the inconsistent time periods removed.

test data and only catches up when nearing the maximum output of 500 W. Why the turbine struggles to produce power during these conditions is unclear; however, this is also the region with the least amount of data, resulting in lower statistical accuracy. At least in some cases, the turbine achieves a similar output to the laboratory test when examining the maximum values within this interval.

After 18 $\frac{\text{m}}{\text{s}}$, the power efficiency of the turbine in the field goes beyond that of the lab, which at first seems like a mistake, but can be explained by the air density. Computing the power coefficient of the field data with the air density found in the lab, the efficiency drops right in between the wind tunnel tests. Since both the turbine in the lab, as well as the one in the field, produce about 500 W due to the hardware limit of the setup, the field turbine only appears more efficient as it generates the same power with less dense air.

Plots of stations 11, 12, 14, and 23 similar to figures 20, 24, and 25 are included in the appendix. For all stations, the overview plot showing station power draw, solar- and wind power, as well as the battery voltage includes a region of uninterrupted records marked in grey, which is necessary for the evaluation in section 3.2.3. When examining the power output and coefficient in relation to the available wind speed of the other four stations, the overall shape and features are very close to the findings in the data of station 13. The time period of station 12 unfortunately does not include any data where the wind speed goes above 20 m/s, so it is not possible to confirm that the power coefficient exceeds the one from the wind tunnel test (see Figure 55). In this regard, station 23 is the only one that shows a similar power coefficient to the laboratory tests at high wind velocities. This station also has the lowest amount of available data, meaning there is a higher uncertainty in its results. Repeating the analysis with a longer time period should clear up how this station behaves.

After compiling the data of all available stations, their power output is fitted with a third polynomial

$$P[W] = a \cdot v^3 + b \cdot v^2 + c \cdot v \tag{16}$$

where the linear term is 0, as no wind power can be generated when no wind is present. All data and fits are graphed together with the wind tunnel test data in figure 28. Their respective fit values are listed in Table 5.

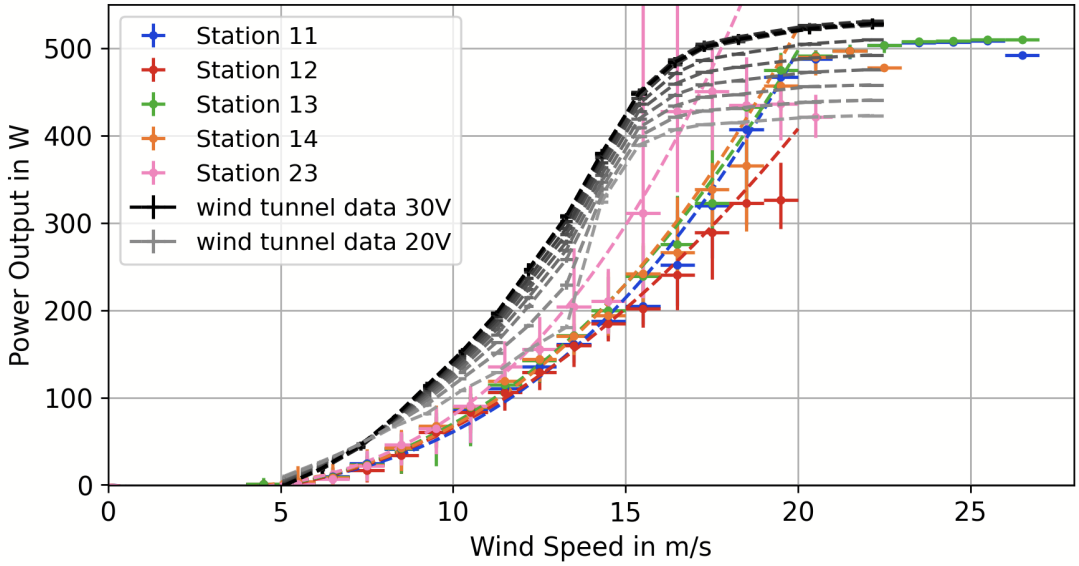

Figure 28: Wind power data of all available stations and the corresponding third-polynomial fits. For comparison, the wind tunnel test data is also shown.

	a $\left[\frac{Ws^3}{m^3}\right]$	b $\left[\frac{Ws^2}{m^2}\right]$	c $\left[\frac{Ws}{m}\right]$
Station 11	0.0480 ± 0.0003	0.442 ± 0.006	-3.14 ± 0.03
Station 12	0.0007 ± 0.0006	1.36 ± 0.01	-7.14 ± 0.07
Station 13	0.0251 ± 0.0006	1.03 ± 0.01	-5.83 ± 0.07
Station 14	0.0451 ± 0.0007	0.59 ± 0.01	-3.66 ± 0.06
Station 23	0.080 ± 0.002	0.36 ± 0.04	-3.6 ± 0.2

Table 5: Fit values for the graphs shown in Figure 28. The error values are taken from the covariance matrix.

All wind turbines generally follow similar curves. Station 23 seems to perform best at low and medium wind speeds; however, the power data available for it is also the most scarce, and thus the errors are the largest as well. Interestingly, its power output drops off roughly 17 m/s, which could be an artefact of low statistics or freezing. Stations 11, 13, and 14 show the limit of 500 W while station 12 never reached it due to the absence of data during very high wind speeds. Station 12 also performs the worst at medium wind velocities.

3.2.3 Energy Storage and Up-Time

A crucial indicator for finding out how much the wind turbines extend the up-time of the RNO-G stations is the energy storage system, in particular, the batteries' charge level. As the stations currently do not have a reading on this specific value, it needs to be calculated manually. As previously discussed in section 3.1.2, the capacity of batteries is dependent on their temperature (see Figure 19). Since the temperature is known at any given time, the real capacity can easily be calculated using the fit values from table 3.

$$Q(t) = Q_0 \cdot (a \cdot T(t)^4 + b \cdot T(t)^3 + c \cdot T(t)^2 + d \cdot T(t) + e) \tag{17}$$

$$Q_0 = 2 \cdot 108\,\mathrm{Ah} = 216\,\mathrm{Ah} \tag{18}$$

Here, the full capacity of the battery array is calculated from the 108 Ah - 100 Hr-rate instead of the 97.6 Ah - 20 Hr-rate, as this better resembles the actual usecase. Although each station uses four batteries, it is only multiplied by 2, since two pairs of batteries are connected in parallel.

When multiplying this time-/temperature-dependent charge capacity by the maximum voltage, one arrives at the energy capacity. As has been said previously, the charging regulator adapts the maximum battery voltage to the temperature as well (Figure 21b). Therefore, the maximum voltage at any given time is calculated using the fit values.

$$E_{\mathrm{cap}}(t) = Q(t) \cdot U_{\mathrm{max}}(t) \tag{19}$$

$$U_{\mathrm{max}}(t) = (-0.060 \pm 0.005)\frac{V}{^\circ C} \cdot T(t) + (28.93 \pm 0.06)V \tag{20}$$

Since both the power inputs (wind and solar power in Figure 20) as well as the station's power expense (station power in Figure 20) are known at any time, these can be integrated over time to compute the energy balance of the system. However, since the batteries can't store an infinite amount of energy, this balance is limited by the actual capacity. In this data-based simulation, the charge state is determined based on these two rules.

Rule 1: If the energy capacity is higher than previously accumulated energy, the effective power generated in the next time interval is added to the energy storage. However, if this amount of energy increases the accumulated energy beyond the capacity of the batteries, the accumulated energy is set to the capacity limit at that time instead.

$$P_{\mathrm{eff}} = P_{\mathrm{Solar}} + P_{\mathrm{Wind}} - P_{\mathrm{Station}} \tag{21}$$

Rule 2: If the energy capacity is lower than previously accumulated energy, there will be no energy added to the system. However, should the capacity drop faster than the power expense can remove energy from the system, the charge state is set to the maximum available capacity instead.

Putting these two rules in a single equation results in

$$E_{\mathrm{accu}}(t + \Delta t) = \begin{cases} \min\left(E_{\mathrm{accu}}(t) + P_{\mathrm{eff}} \cdot \Delta t,\ E_{\mathrm{cap}}\right) & \text{if } E_{\mathrm{cap}} \geq E_{\mathrm{accu}}(t)\,, \\ \min\left(E_{\mathrm{accu}}(t) - P_{\mathrm{Station}} \cdot \Delta t,\ E_{\mathrm{cap}}\right) & \text{if } E_{\mathrm{cap}} < E_{\mathrm{accu}}(t)\,. \end{cases} \tag{22}$$

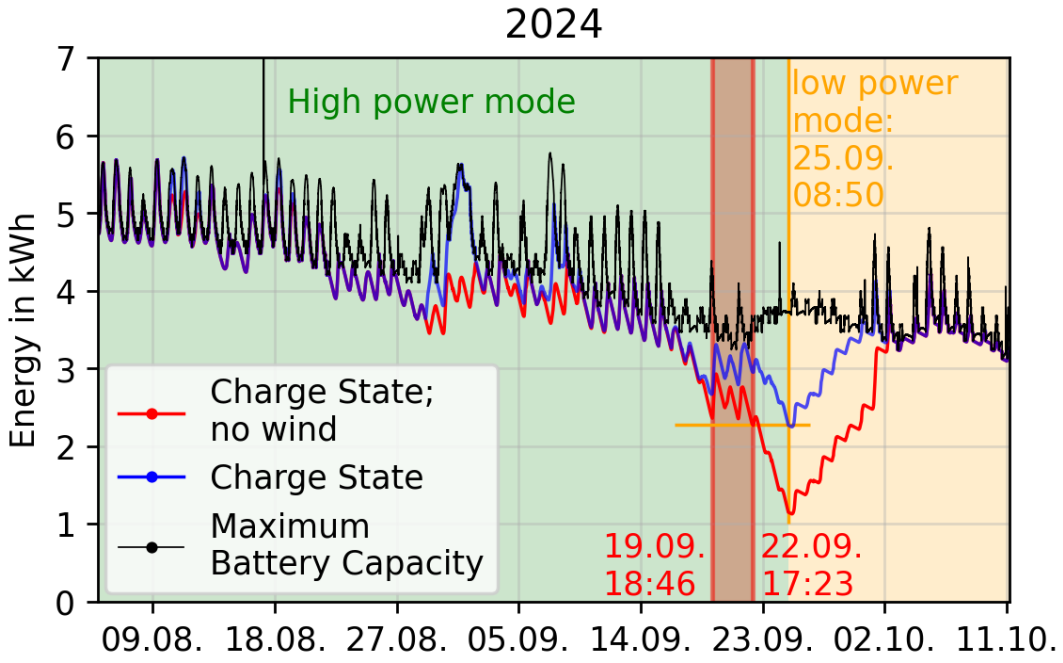

Figure 29: Battery capacity and charge state are calculated with equations 19 and 22 based on the input and output power as well as the temperature measured inside the battery compartment. Similarly, the theoretical charge state without wind power is calculated by removing P_{Wind} from P_{eff} in equation 22. Marked in red are two instances where the station would need to be switched to low power mode.

The graphs in Figure 29 are the results of this computation. By construction, the charge state cannot exceed the maximum battery capacity, as can be clearly observed. In the beginning, the batteries are still comfortably charged to their maximum capacity, whereas in later times, the solar power struggles to charge them fully. Fortunately, there happened to be strong winds during that time, keeping the station charged for about two days. Eventually, the winds died down, and with less and less solar energy, station 13 had to be shifted into low power mode on September 25 at 08:50, meaning no radio signals are processed, stopping any search for neutrinos. Even though the charging regulator tries to compensate for the capacity loss due to decreasing temperature by increasing the maximum voltage, it cannot counteract the effect entirely, resulting in peaks and troughs in energy capacity, mimicking the day-night cycle.

Since the charge state is calculated manually, it allows for the computation of a separate theoretical charge state, where only the solar panel delivers power. This demonstrates how much the turbine contributes to the energy balance. Furthermore, by finding a similar charge level at which to shut down the station's data-taking components, the up-time increase due to wind power can be estimated. As the red region in Figure 29 suggests, removing the wind power from P_{eff} in equation 22 reduces the up-time by 2.5 to 5.5 days.

To gain insight into what could become possible in the near future, the station's power draw can be reduced in the simulations. Figure 30 shows three examples with reduced

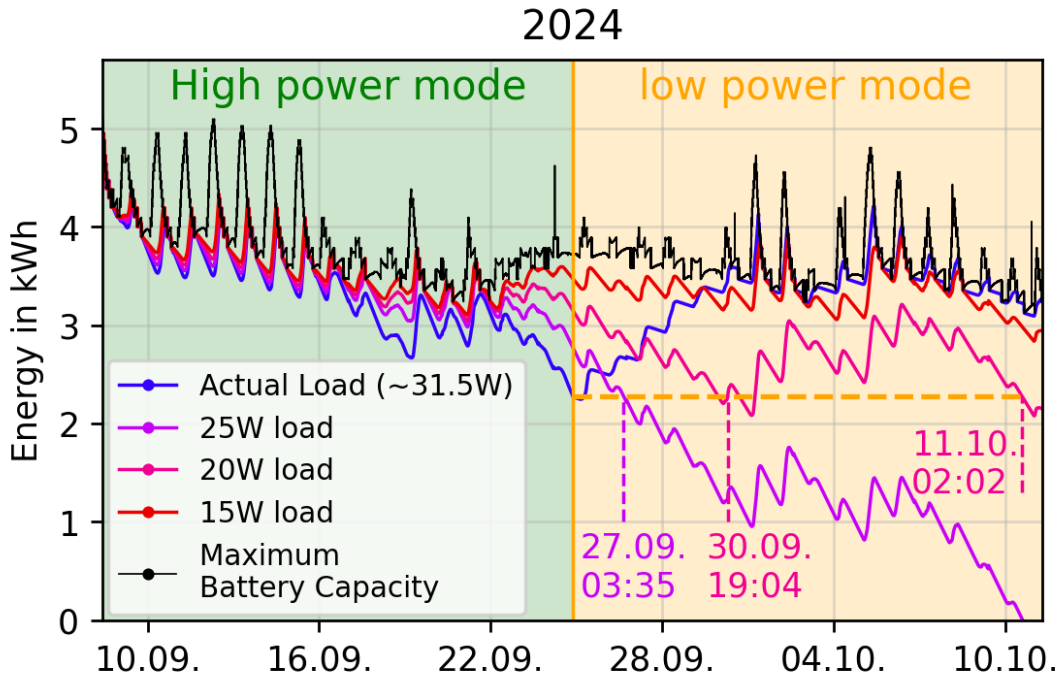

Figure 30: Comparing simulated power draw of 25 W, 20 W, and 15 W to the real data of station 13. For 25 W and 20 W, the dates when they would switch to low power mode are marked.

requirements. None of them change their power mode when crossing the threshold on 25.09. to see how they would perform after that date. For a power requirement of 25 W, the up-time does not increase significantly, only lengthening by just under two days, which is close to the up-time increase the turbine provides. Lowering the output power even further to 20 W, one can see an immense improvement. On September 30, 5.5 days after the real station switched to low power mode, the simulation crosses the charge state threshold for the first time. However, after recovering for a bit, due to the strong sunlight, the simulation again falls below 2.28 kWh on October 11, potentially having an immense up-time increase of half a month. For a station that draws 15 W, the up-time seems to be indefinite in Figure 30. All the same, it will reach the point where no sunlight is available whatsoever, leaving the ever-so-important task of powering the station solely to the wind turbine. Unfortunately, since there is no power data beyond this, when exactly this simulated station would need to change power mode cannot be calculated.

3.3 Wind Power Review and Future Plans

Analysing the available and produced wind energy of the stations shows, both the power output and output efficiency follow a similar curve to the controlled lab testing. However, there are several features that are not present in the test, such as the unexpected low efficiency coefficients between 8 and 11 m/s wind speed, as well as the low power output for wind speeds between 10 and 18 m/s. In July 2025, a new, bigger WT14 turbine with

a swept area of 1.5 m^2 was installed at station 12, replacing the smaller WT10. This new turbine shows promising results in the first tests after installation, reaching a power output of 300 W with a wind velocity between 10 to 12 m/s in the field. This could be a good leap forward considering the second part of this analysis, where it is shown, that the smaller turbine already lengthened the up-time of the station by several days and in a hypothetical, but very possible, scenario of a less power demanding station, could have increased the up-time by about 16 days. With a turbine producing about double the power, this could have an even greater impact, should the generated energy be enough to supply a station until the next strong wind period and so on. This also opens the door to the possibility of temporarily switching on the stations during high wind periods in the middle of winter, extending the uptime even further. However, for the data taken during high wind periods to be of any real use, the problem of increased noise in the radio frequency spectrum during said periods needs to be elevated as well.

4 Acoustic Background Tagging

The previous chapter focused on the first part of the goal this thesis aims to achieve: analysing the wind power input and energy balance of the stations to improve the uptime of the detector with future upgrades, ultimately increasing the sensitivity of the array. Not only is it essential to keep the RNO-G stations running, but it is also crucial to minimise background noise in order to achieve the most accurate measurements possible. An interesting aspect of RNO-G's signal integrity is that it seems to be affected by high wind speeds. A correlation, if not a perfect one, can be seen between wind speed and trigger rates. This reduces the detector's sensitivity by clouding real neutrino signals with false-positive events generated by the weather. Therefore, understanding the source of these events is necessary to either eliminate them entirely or find a way to reject the non-neutrino events.

4.1 The Triboelectric Effect

The first records of electric field magnitudes (EFM) generated by winds blowing over snow stem from G. C. Simpson, which were taken with a near-surface electroscope during an Antarctic expedition between 1911 and 1913 [27]. This effect is theorised to be the leading cause of many background events during intense wind periods. Although the exact mechanism is not entirely understood, it is believed that the rapid coronal discharge of the built-up electric field causes radio pulses mistaken for actual neutrino signals in the detector. According to [28], all radio neutrino detectors included in their research (ANITA, ARIANNA, RICE, AURA, SATRA, ARA, RNO-G, and TAROGE-M) show increased activity during high wind speeds. Notably, the threshold behaviour discovered by G. C. Simpson, in which the electric field increases dramatically only after a specific wind velocity is exceeded, parallels the behaviour of neutrino detectors, which coincidentally register increased event rates above a given turn-on wind speed. While the precise threshold varies depending on the antenna and trigger choice, all aforementioned radio neutrino experiments measure increased rates above 10 m/s [28]. Figure 32 shows an example of increased event rates at RNO-G detector stations. This is consistent with the onset wind speed found by G. C. Simpson of about 6 to 8 m/s (see Figure 31). This presents a huge problem, as simply disregarding all data taken when the wind speed is above 8 m/s or 10 m/s reduces the effective uptime by 19.6 % or 8.9 % respectively, suggested by the wind occurrence data shown in Figure 33. The darker regions indicate instances where the wind speed is > 8 m/s or > 10 m/s, respectively. This would be a significant detriment to the sensitivity of the detector and the goal of the RNO-G collaboration of detecting neutrino flux in the ultra-high energy region. Additionally, high wind speeds offer the only opportunity for the detector to function during winter, as they are the sole power source available at that time. Disregarding all data taken during the winter would also dramatically reduce the uptime, forcing the experiment to run about twice as long as needed. To emphasise this, at energies $\gtrsim 100$ PeV, the diffuse cosmogenic neutrino flux is only in the order of one event per 10 km^3 of sensitive detector volume *per year* [12]. Therefore, the importance of reducing the downtime of the detector can not be stressed enough.

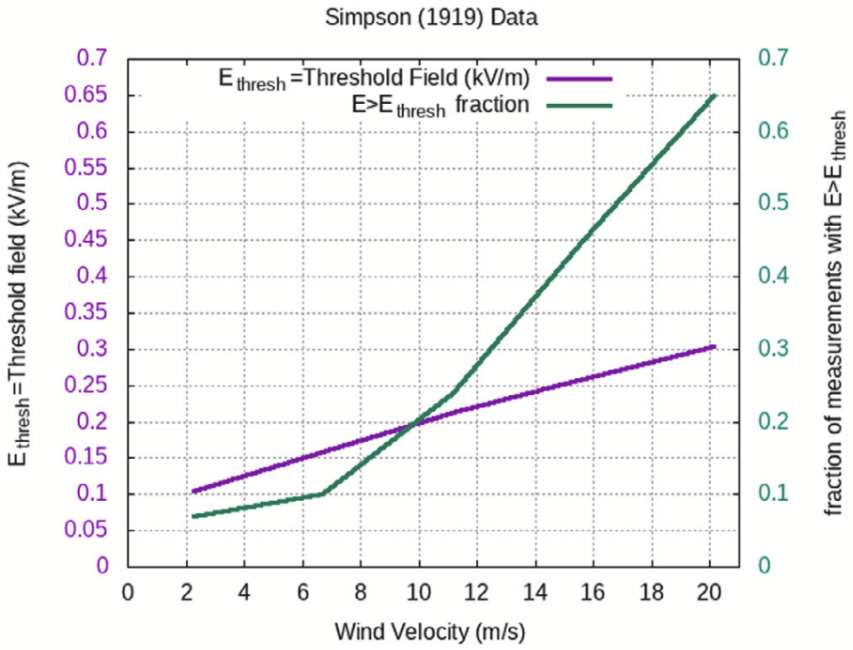

Figure 31: Original data from G. C. Simpson in [27], graphed in [28]. Left Scale: Electric field threshold to reference the measurements. Right Scale: Fractional occurrence frequency of electric fields exceeding the threshold.

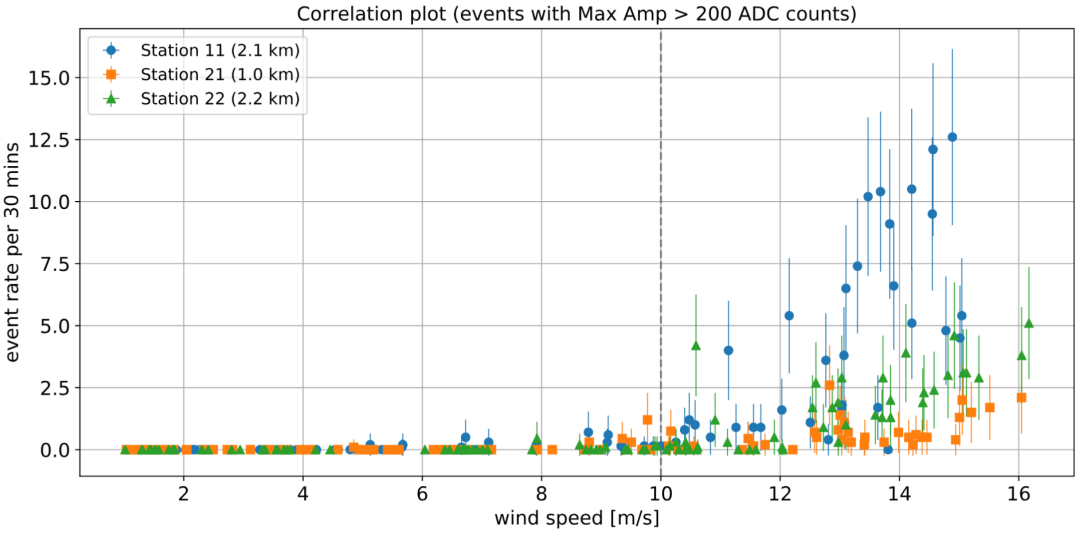

Figure 32: Event rate of RNO-G station 11, 21, and 22 over wind speed. The grey dashed line signifies the threshold velocity after which the stations show increased event rates. Figure from [28].

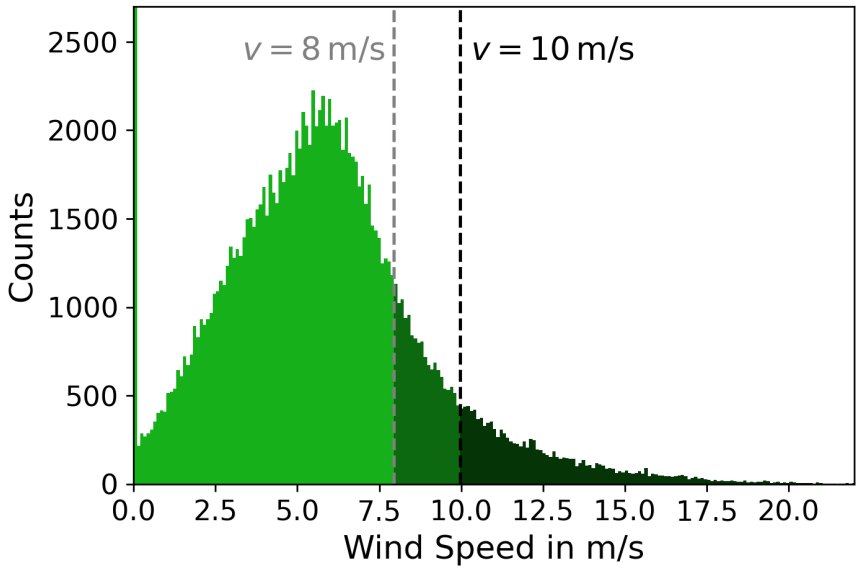

Figure 33: Histogram of the wind speed measured by NOAA between 31.12.2009 at 23:00 and 31.12.2024 at 23:00 (averaged over one hour) [6]. Every instance where the wind speed is $> 8\,\mathrm{m/s}$ is shaded in a darker green, while everything $> 10\,\mathrm{m/s}$ is shaded even darker.

4.2 Experimental Setup

With such minuscule flux, one can not rely on statistics alone. If an event is recorded, it must be ensured that it is from an actual neutrino and not a background signal. Multiple independent criteria should be used to determine this, one of which might be acoustic noise. For example, if an acoustic signal accompanied radio signals generated through the triboelectric effect, events recorded simultaneously with such an acoustic pulse could be rejected. To determine if acoustics are related to the increased trigger rates of the detector at all, an experimental setup is constructed. The setup is powered by a single 12 V lead acid battery with no power generation (see Figure 34). Therefore, two runs are performed, where the battery is charged in between at the campsite. The 12 V from the battery are converted using DC-DC converters to 5 V for supplying power to the Raspberry Pi-4, 6 V to power the glaciophone, and 3.3 V for the differential signal output of the glaciophone. The glaciophone is a repurposed HTI-92-WB hydrophone from High Tech Inc. [29] recovered from the AMADEUS project [30]).

The perfboard on the right is utilised for voltage conversion and is both designed and built by the electronics workshop of the FAU (see Figure 35).

The left perfboard houses a Raspberry Pi-4 with an AD HAT by Waveshare [31], which is equipped with a Texas Instruments ADS1263 ADC [32]. The two rightmost terminals provide 5 V reference voltage from the Raspberry Pi, which is used to create a 2.5 V level through a voltage divider. The differential signal of the glaciophone is cleaned with input capacitors and referenced to the 3.3 V of a DC-DC converter. A circuit diagram is shown in Figure 36

Afterwards, the two signals are sent to the ADC HAT's pins IN0 and IN1. All other

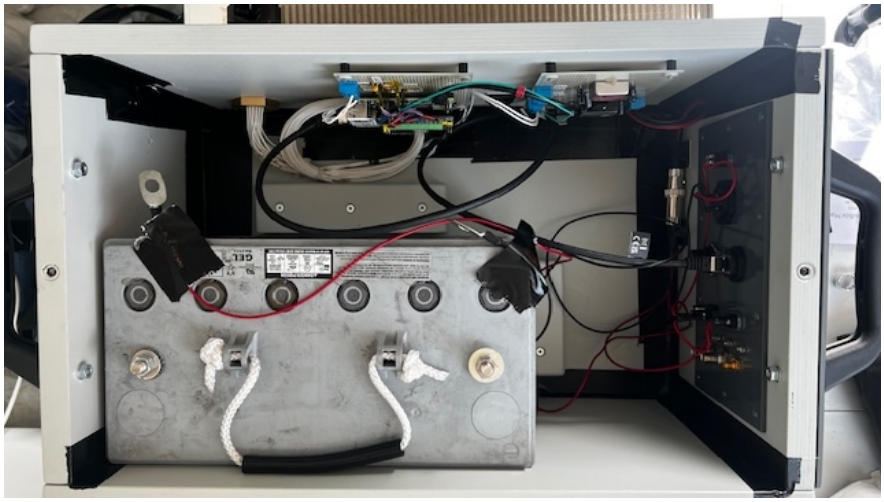

Figure 34: Fully assembled electronics for measuring the acoustic background noise.

input pins are set to the previously mentioned 2.5 V voltage, as instructed in the ADC's manual. Lastly, the glaciophone is connected to the electronics through a Seacon AWQ 4/24 ALL-WET series bulkhead connector [33] on the outside of the enclosure. When deployed, communicating with the computer remotely is not possible. Instead, the data is extracted after recovering the experiment by plugging directly into the RJ45 connector on the front panel and logging in to the Raspberry Pi with SSH.

The entire setup needed to be conceptualised, built, and tested very quickly to be brought to the next flight to Greenland's Summit Station, which is why the glaciophone was not calibrated. Instead, all data taken is presented in arbitrary units.

In anticipation of a high wind period, the experiment was deployed for the first time near station 13 of the RNO-G detector by Felix Schlüter and Jason Chan on 31.05.2025. The glaciophone was buried in the snow at a depth of about 0.5 m as seen in Figure 37, while the enclosure, which contains the necessary electronics and battery, was placed on top of a wooden plank on the surface. During this first run, the box was covered with a plastic bag to protect it from the harsh conditions, which was deemed unnecessary for the second one. After retrieving the experiment and recharging the battery, it was again deployed on 12.06.25. Picture 38 shows how the experiment looked at retrieval after the first run. The wind dragged snow across the open field, nearly covering the experiment fully. For this eventuality, rods have been placed to mark the position of the experiment.

4.3 Data Acquisition

The code for the data acquisition runs in C and uses mostly prewritten functions provided by the manufacturer of the AD HAT. The Raspberry Pi records the input noise picked up by the glaciophone at a constant rate of 19.2 kHz. This limits the available frequency spectrum to 9.6 kHz as required by the Nyquist–Shannon sampling theorem [34] to avoid aliasing. In principle, the ADC is capable of sampling rates of 38.4 kHz. However, this significantly reduces the accuracy of the data. The setup records data continuously while every 11520000 samples, or in other words, every ten minutes, a new

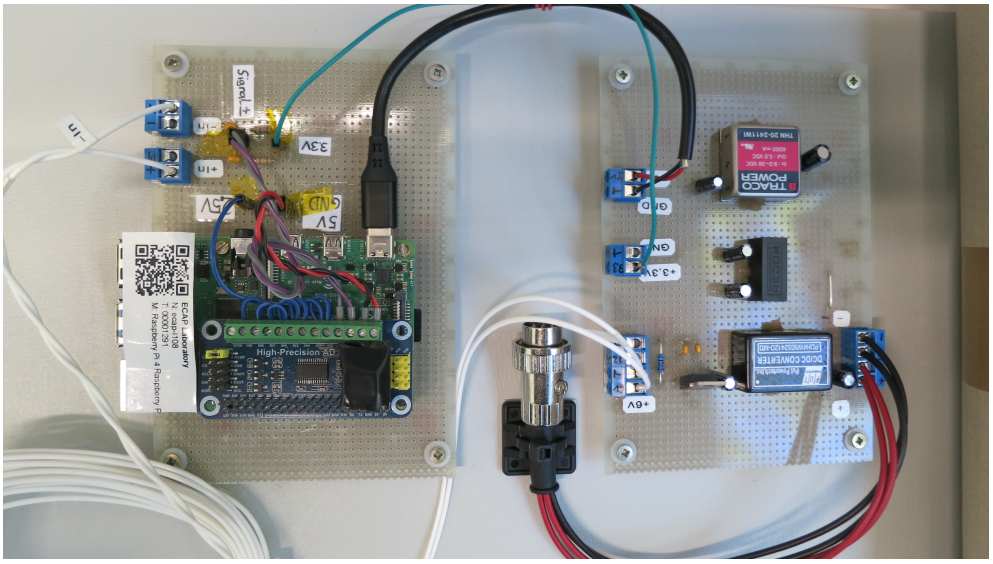

Figure 35: The right perfboard is used for the DC-DC conversion from 12 V to 3.3 V, 5 V, and 6 V. The left perfboard is used for differential data acquisition from the glaciophone, utilising a Raspberry Pi 4 and an ADC-HAT. The Micro-Computer is also equipped with a real-time clock, which malfunctioned in the cold environment of Greenland.

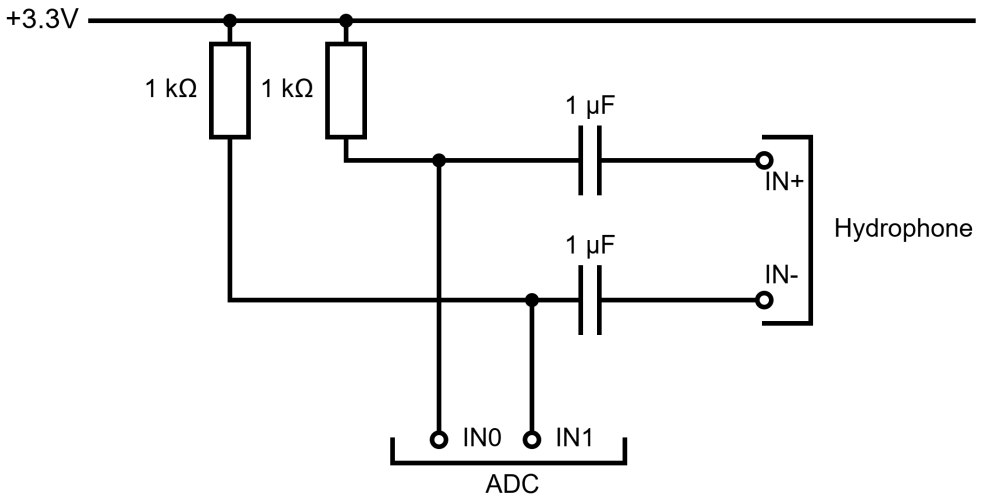

Figure 36: Input signal circuit connecting the glaciophone to the ADC HAT.

Figure 37: Deployment of the acoustic noise measuring equipment. The enclosure is placed on a wooden plank on the surface, while the glaciophone is buried in snow at a depth of about 0.5 m. Picture taken by Felix Schlüter.

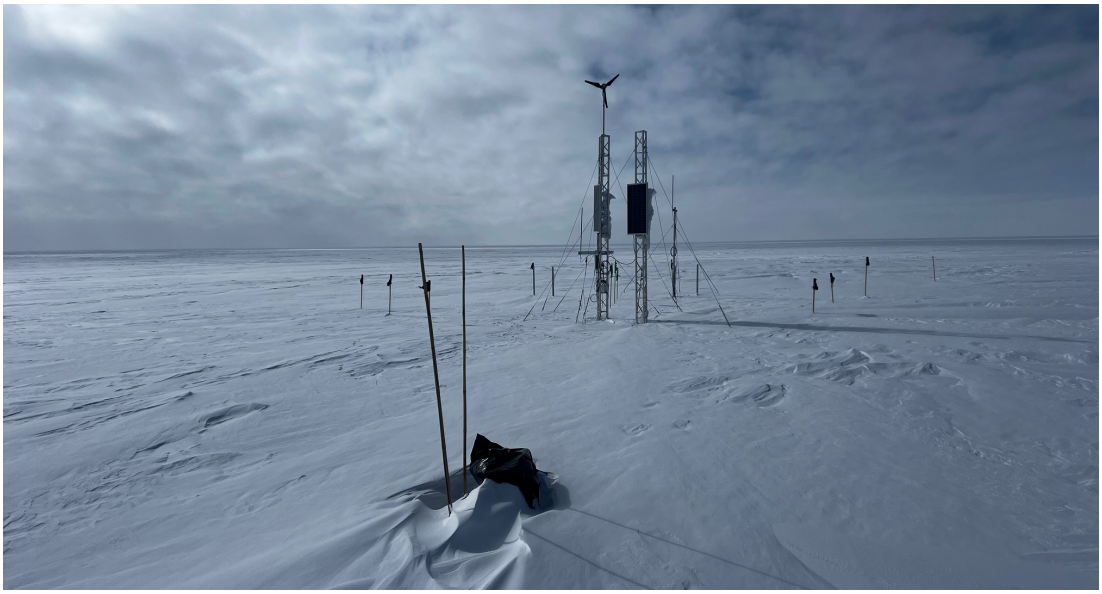

Figure 38: Experimental setup in front of station 13 at retrieval after the first run. Picture taken by Felix Schlüter.

file is created, and the previous one is saved to an SD card. The differential signal of the probe is saved in a binary file and translated during evaluation. As mentioned in the previous subsection, two measurement runs have been carried out. The first one went

from 31.05.2025 - 15:48 to 06.06.2025 - 17:47, while the second started on 12.06.2025 - 11:00 and ended on 14.06.2025 - 18:31. Dates are given in Western Greenland Summer Time (WGST), which is UTC-1. To synchronise the measurements of the glaciophone with the wind speed and trigger rate readings of the RNO-G stations, the Raspberry Pi had been equipped with a real-time clock (RTC). Unfortunately, due to the extreme cold, the RTC malfunctioned. Therefore, determining the absolute time of the measurements relies solely on the written notes of the deployment team, which consisted of Felix Schlüter and Jason Chan.

4.4 Data Processing

The intermediate goal of this subsection is to extract the sound signal recorded by the glaciophone depending on frequency. The acoustic energy of a signal can be expressed in the most general terms as the integral of the signal strength over all time.

$$E_{\text{Signal}} = \int_{-\infty}^{\infty} |s(t)|^2 dt \ , \tag{23}$$

where s(t) is the signal strength at time t. However, since the signal data is to be analysed in multiple frequency intervals, a Fourier transform is performed on the signal strength

$$\hat{s}(f) = \int_{-\infty}^{\infty} e^{-i2\pi ft} s(t) dt \ . \tag{24}$$

When assuming that the energy in the signal is finite, Parseval's theorem can be applied (see equation 25). This allows for the computation of the signal energy in the frequency domain instead.

$$\int_{-\infty}^{\infty} |s(t)|^2 dt = \int_{-\infty}^{\infty} |\hat{s}(f)|^2 df \tag{25}$$

$$E_{\text{Signal}} = \int_{-\infty}^{\infty} |\hat{s}(f)|^2 df \tag{26}$$

The integral can be limited when calculating the energy of a given frequency interval.

$$E_{[f_j, f_k]} = \int_{f_j}^{f_k} |\hat{s}(f)^2| df \tag{27}$$

When applying this to the sampled dataset, a fast Fourier transform (FFT) is used rather than a continuous Fourier transform to ease computational load, and so the integral becomes a sum instead

$$E_{\text{Signal}} = \sum_{i=1}^{n-1} |\hat{s}(f_i)|^2 \ . \tag{28}$$

In this specific calculation, a bin value of 1024 entrances is used. Since only positive frequencies are of interest in this scenario, the usable bins are reduced to 512, and thus the transformed signal has a resolution of 18.75 Hz.

$$f_i - f_{i-1} = \frac{\text{Frequency Range}}{\text{Bins}} \tag{29}$$

$$= \frac{\frac{\text{Sampling Rate}}{2}}{\text{Bins}} = \frac{\frac{19\,200\,\text{Hz}}{2}}{\frac{1024}{2}} = 18.75\,\text{Hz} \tag{30}$$

According to the Nyquist-Shannon sampling theorem, the frequency range is reduced to half of the sampling rate. Similar to equation 27, calculating the energy in a frequency interval while using the discrete FFT can be expressed as

$$E_{[f_j,f_k]} = \sum_{i=j}^{k} |\hat{s}(f_i)|^2 \quad \text{where } f_i = i \cdot 18.75\,\text{Hz} \tag{31}$$

As stated before, the experiment is set up to save individual files every 10 minutes automatically. The contents of each of these files are converted from binary to ASCII separately and transformed to frequency space using the method above. Since the RTC malfunctioned, the time stamps for each file are corrected utilising the written notes as a starting point and calculating the absolute time of each file with the knowledge that all files are created in 10 min intervals.

4.5 Analysis of the Acoustic Noise Signals

After discussing how the data is acquired and processed, it can finally be analysed to see whether acoustic noise holds any information about the trigger rate increase during periods of high wind. A histogram of the wind speed recordings during the two runs is shown in Figure 39.

As properly calibrating the glaciophone was impossible due to tight time constraints, all subsequent analyses based on the measured loudness are presented in arbitrary units and should be regarded as qualitative. Figure 40 shows the calculated energy in the frequency range between 0.5 and 9.5 kHz of the first run. It identifies two single-point outliers that will be removed from the dataset. The biggest reading, including both runs, is also found in the first run, which is chosen as a reference point to normalise the rest of the data.

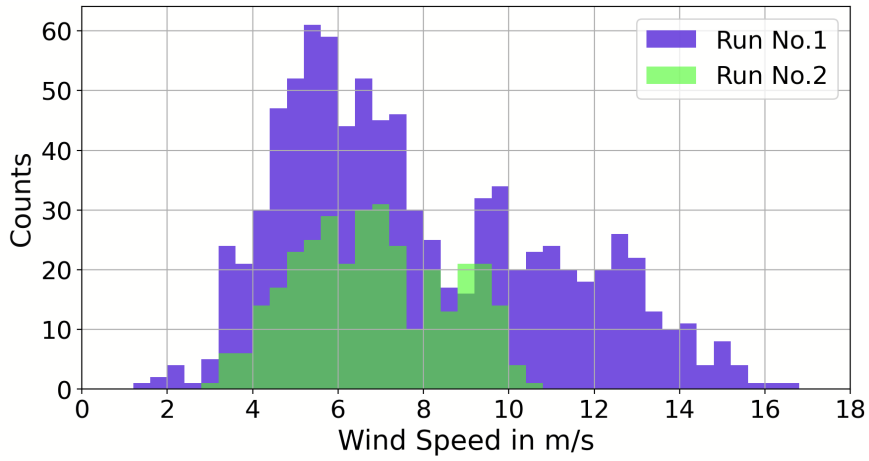

Figure 39: Histogram of the wind speed measurements during the first and second run. The first took place between 31.05.2025 - 15:48 and 06.06.2025 - 17:47, while the second run went from 12.06.2025 - 11:00 to 14.06.2025 - 18:31.

The normalised data of the first and second run, as well as the wind speed data, can be seen in Figure 41. It can be observed that the wind speeds do not reach as high in

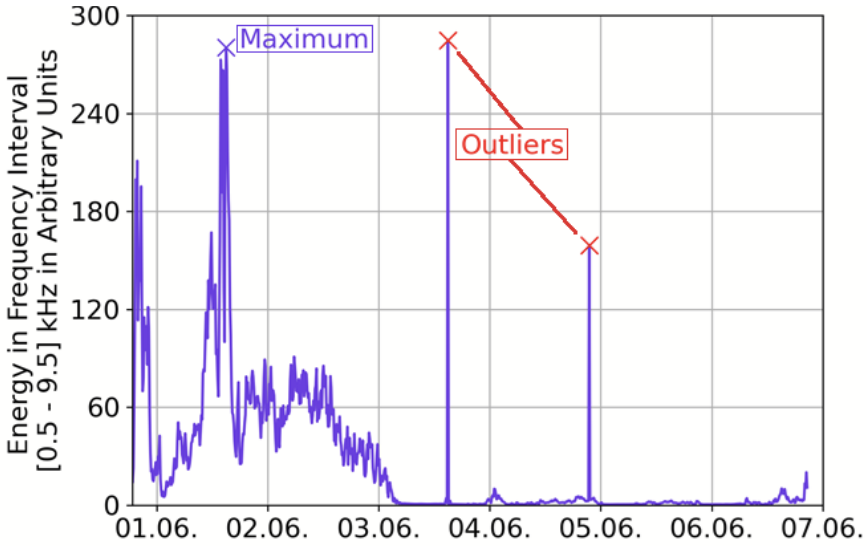

Figure 40: The calculated, un-normalised, and uncalibrated energy reading of the glaciophone during the first run shows two outliers, which are removed from the data set, and the maximum value of the whole experiment.

the second run as in the first, contributing to the much lower relative noise volume. However, the most critical factor for the lower noise readings is probably the absence of a plastic bag in the second run, which had covered the electronics during the first deployment.

Nevertheless, plotting the acoustic noise over the associated wind speed, it is clear that the noise increases with stronger winds in both runs, as expected (see Figure 42). As mentioned previously, the second run demonstrates an overall lower noise, but it still increases with wind speed. Interestingly, the noise increase appears to begin at a velocity of 6-8 m/s, which corresponds to when the wind turbine starts turning. Whether this is a coincidence could only be determined by comparing the noise data with the RPM or the wind power generated by station 13, near which the glaciophone had been placed. Unfortunately, the power data is unavailable for the time period during which the acoustic tests were performed, and the RPM readout is not yet functional. This test could be repeated in the future while station 13 is operational, and ideally when the RPM readout function is fully implemented.

Dividing the noise energy into several frequency intervals reveals the most problematic frequencies as seen in Figure 43. For run No.1, the loudest frequency range is 3.5-4 kHz, while in run No.2 it is 1.5-2 kHz. The higher pitch during the first run can be a consequence of the higher wind speeds, but is most likely also a result of the plastic bag rattling in the wind. It is important to note that the colour scale changes between runs to account for the lower noise in run No.2.

Lastly, and most importantly, the correlation between the trigger rate, wind speed, and acoustic noise volume is analysed with Figure 44. As one can see, the trigger rate depends on both the wind speed and the acoustic noise, which is not surprising, considering the relative energy in the measured frequency range depends on the wind speed itself, as Figure 42 suggests. While run No.1 shows a significant rise in trigger

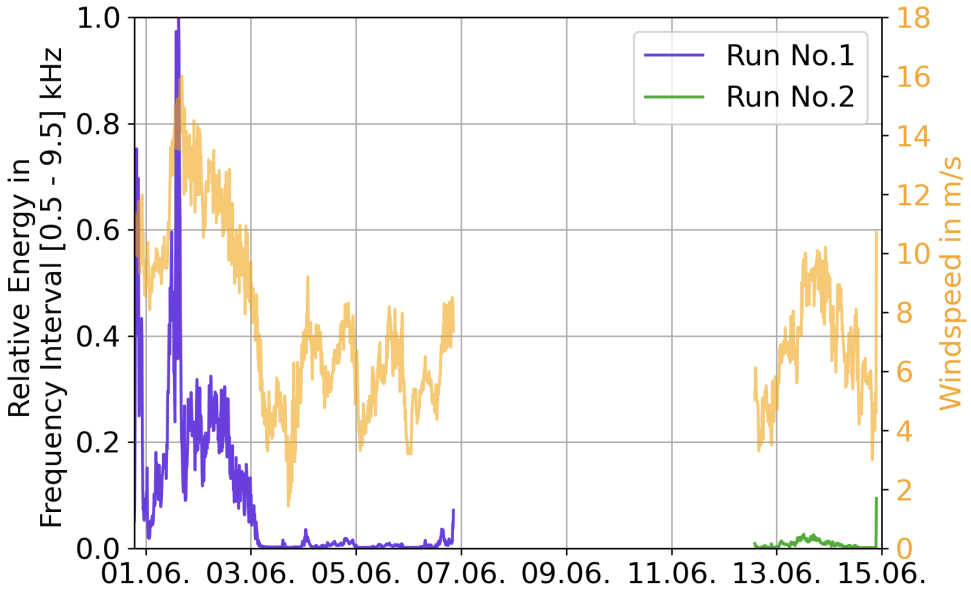

Figure 41: Normalised acoustic energy of the first and second run together with the wind velocity readings.

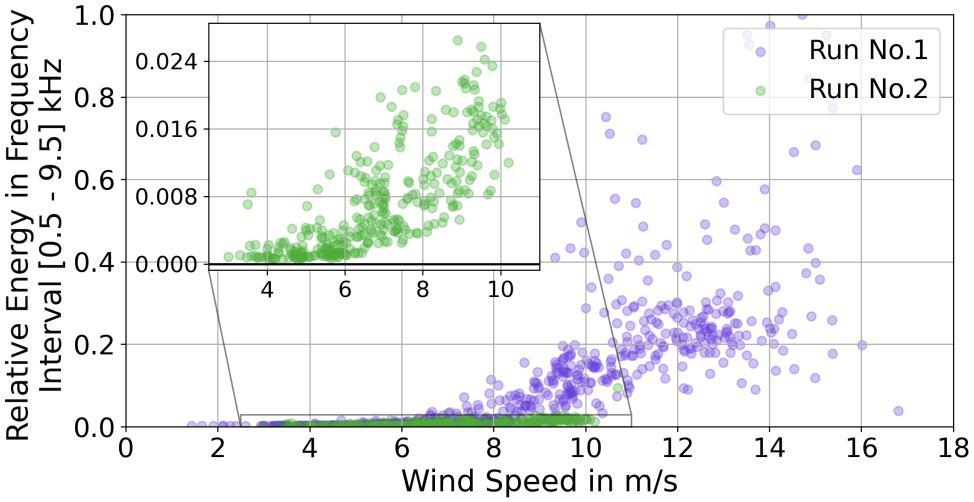

Figure 42: The plots show the acoustic noise increase of the first and second runs with stronger winds. The second run shows lower noise overall due to the missing plastic bag that covered the experiment in run No.1.

	Pearson Coefficient		
	Acoustic Noise vs. Wind Speed	Trigger Rate vs. Wind Speed	Trigger Rate vs. Acoustic Noise
Run No.1	0.762	0.535	0.300
Run No.2	0.680	-0.188	0.042

Table 6: Pearson coefficients for the two plots shown in Figures 42 and 44

rates with higher wind speeds and acoustic noise, the second does not. This might be attributed to lower velocities at the time of recording. Run No.1 shows an almost threshold-like behaviour, where the trigger rate increases massively above $\sim 10\,\mathrm{m/s}$, which was never surpassed in the second run. The Pearson coefficient is used to quantify the correlation behaviour, which is calculated according to equation 32 [35].

$$\rho_{\mathrm{Pearson}} = \frac{\sum_{i=1}^{n}[(x_i - m_x)\cdot(y_i - m_y)]}{\sqrt{\sum_{i=1}^{n}[(x_i - m_x)^2]\cdot\sum_{i=1}^{n}[(y_i - m_y)^2]}} \tag{32}$$

Here, x and y represent the individual data sets, for example, the wind speed on the x-axis and the trigger rate on the y-axis, while m_x and m_y are the means of those data sets, respectively. For a Pearson value >0, a direct proportionality is observed. Vice versa, a negative Pearson value represents a negative correlation. The closer the absolute value of the coefficient approaches 1, the stronger the correlation is. However, since the Pearson coefficient measures the normalised covariance, it can only represent a linear correlation and does not account for other dependencies. Therefore, this approach is limited but is sufficient to determine if acoustic noise indicates the source of the disruption in the trigger rates.

The coefficients for the plots in Figure 44, as well as the wind speed to audible noise correlation from Figure 42, are written in Table 6. From the four values, it becomes clear that there is a much higher correlation between the trigger rate and the wind speed in the first run. In contrast, in run No.2, there is almost no correlation in both plots, and even the opposite of what is expected when comparing the trigger rate to the wind speed. This could again be attributed to the lower wind speed in the second run. Almost all unreasonably high trigger rate events happen above 10 m/s, which is not reached in the second run.

When examining the first run in the bottom plot of Figure 44, it is immediately revealed that the highest relative acoustic noise does not coincide with the highest trigger rates. This can also be seen in the top plot of Figure 43, where both the audible noise measurement and the wind speed reach their maximum approximately 6 hours before the trigger rate rises rapidly. It has to be said that this time frame exhibits extreme behaviour in that regard. Inspecting all the available wind speed and trigger rate data, which spans from 24.04.2023 up to 17.09.2025 (shown in Figure 45), and shifting the trigger rate in time with respect to the wind speed recordings while optimizing for the resulting Pearson coefficient gives a time shift of $\Delta t = 2.8\,\mathrm{h}$, meaning the spikes in the trigger rates are on average delayed by nearly 3 h. The time period of the first run using the glaciophone is shown in Figure 46 while the Pearson coefficient for different time shifts is shown in Figure 47. Whether there is a technical reason for this delay, such as time-keeping issues, or if this is a systematic behaviour of the detector, is not resolvable

in this limited examination. It is again possible that the geometric evaluation through calculating the Pearson coefficient does not represent the data well. Thus, this attribute needs to be studied further by explicitly looking for this lagging phenomenon in more detail. It is important to note that Figure 45 shows trigger rates are sometimes less or not at all impacted by high winds, which currently can not be explained. Both features might be explainable when the mechanism behind the radio noise signals is understood.

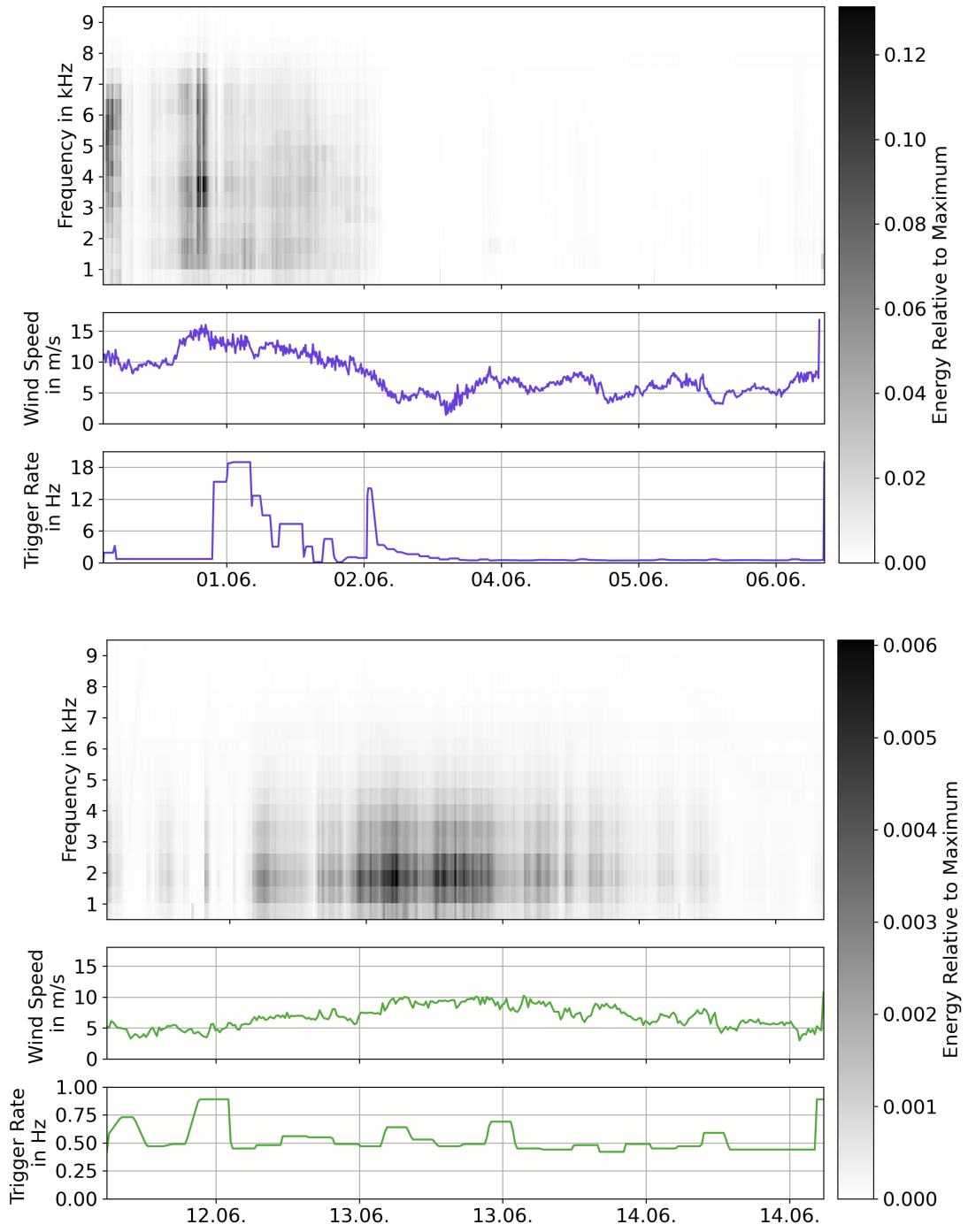

Figure 43: The data from both runs is shown in multiple frequency ranges to discover which shows the loudest noise during the tests. The top plots show run No.1 and the bottom ones show run No.2. The wind speeds and trigger rates are also presented for each.

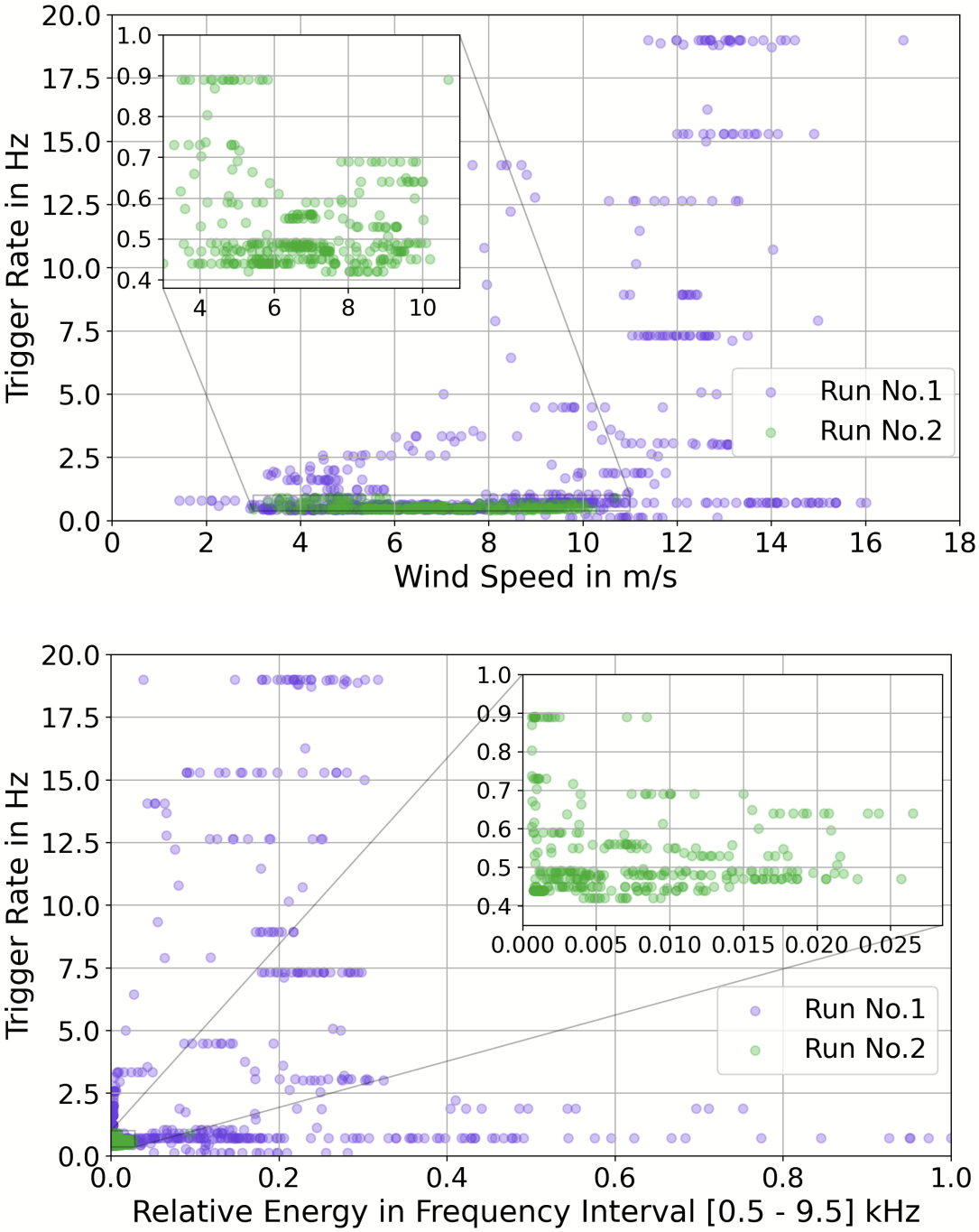

Figure 44: The top plot shows how the trigger rates of both runs change with wind velocity. The bottom plot displays the same trigger rate samples but over the relative acoustic noise volume.

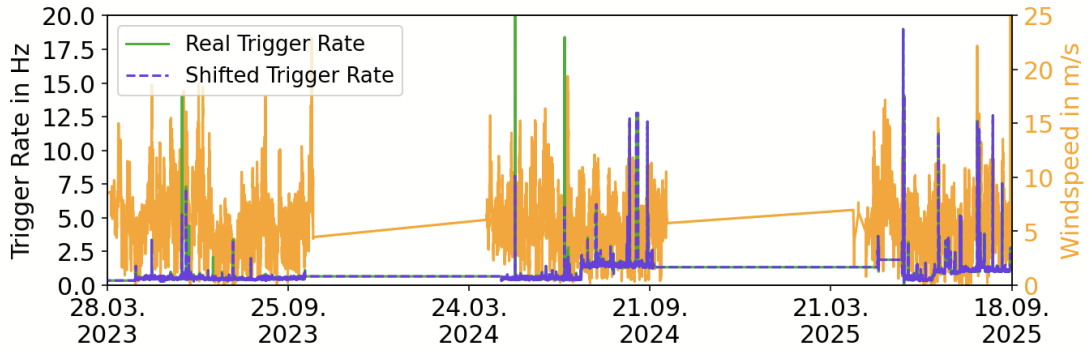

Figure 45: All trigger rate data of station 13 and wind speed.

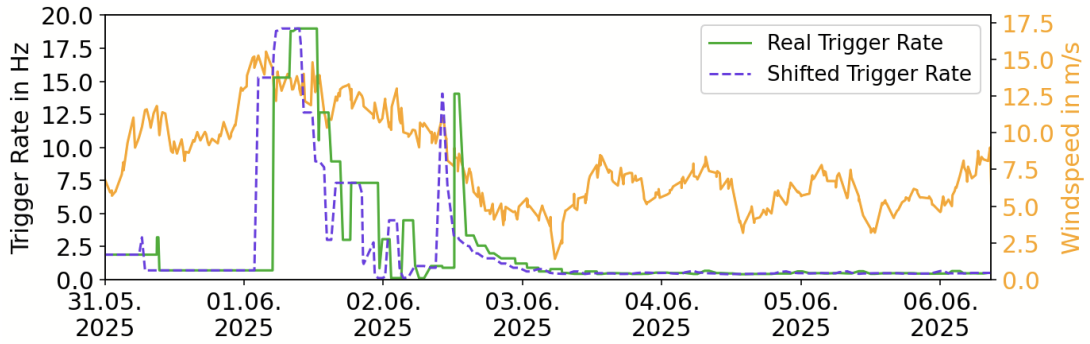

Figure 46: Trigger rate data (real and shifted by 2.8 h) of station 13 and wind speed during the first measurement period, where the glaciophone was deployed.

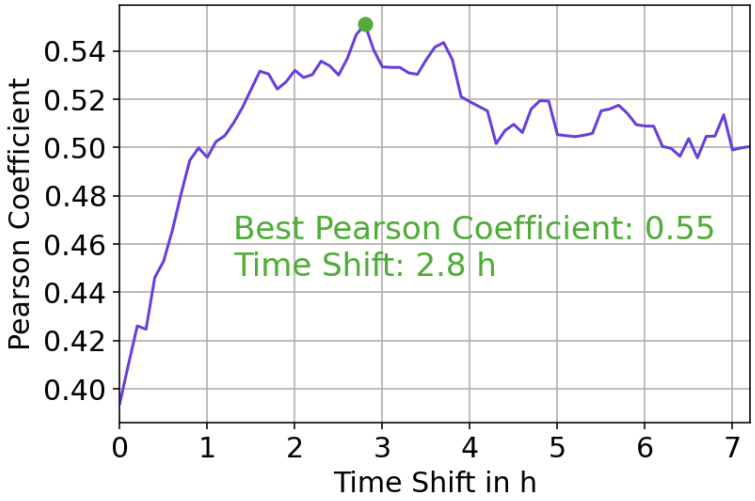

Figure 47: Pearson coefficient between the trigger rate and the wind speed, depending on the time shift applied to the trigger rate.

5 Conclusion

In this thesis, two key aspects relevant to the sensitivity of the Radio Neutrino Observatory in Greenland (RNO-G) are examined: the uptime of the detector stations and, especially, how wind power contributes to it, as well as the identification of wind-induced noise signals that create false-positive radio neutrino events. The first goal of this work is to evaluate the effectiveness of power generation from turbines at the stations and how they could provide the necessary energy during winter, when no supplementary solar power is available. The second goal is to determine whether acoustic noise is an indicator of the disturbances in the trigger rates of the detector. In order to achieve the first objective, a replica of the power system used with RNO-G stations is built on the roof of the Erlangen Centre for Astroparticle Physics (ECAP). This station will not only be usable for comparing power generation efficiency with the turbines in the field but will also serve as a testing ground for future hard- and software upgrades. This avoids the risk of reducing the uptime of the actual detector stations should any new revisions fail to perform immediately. The power system test station features the same WT10 turbine and a similar single 100 W solar panel, both of which generate power and store it in four 97.5 Wh lead-acid batteries. Communicating with the station is facilitated by an Ethernet connection to the local network of the ECAP. The system includes the Tidy-Power board, controller board, as well as the RADIANT (**RA**dio **DI**gitizer and **A**uxiliary **N**eutrino **T**rigger), all of which are designed by the RNO-G collaboration. While these are typically used for long-term neutrino astronomy, they are used here only to monitor power generation at the moment. Shifting focus to the power data from RNO-G stations, the five stations which are equipped with a turbine (11, 12, 13, 14, and 23) are inspected for their ability to generate power from wind. This includes their power output as well as their power coefficient - the efficiency with which wind energy is converted into usable electric energy. All stations generally follow the same curve for both output power and efficiency and are comparable to wind-tunnel tests conducted with the WT10 turbine. However, there seem to be some unexpected aspects where all the turbines sometimes display very low power generation efficiency up to a wind speed of about 11 m/s. One such period is discussed in detail, though the cause of such events can only be theorised at this time. A possible explanation is the icing on the turbine preventing it from spinning. Unreasonably low efficiency coefficients are not observed at higher wind speeds, as these allow the ice to break off, freeing the turbine and allowing it to spin. Using the power data from each station, it is possible to calculate each station's battery charge state to examine up-time and how the turbines contribute to it. For this, the charge state is calculated with and without wind power. Comparing these two reveals how much earlier a station would have to be shut down before the batteries would have drained too far. For station 13, this amounts to an increase in up-time of 2.5 to 5.5 days, while station 11 lasted 1 day longer. For stations 12 and 23, the necessary data was not recorded, while station 14 was put in low-power mode prematurely. Another calculation was performed using the actual generated power with theoretical loads of 15, 20, and 25 W. This gives an idea of how a future revision of the detector station could perform when using less power. While a 25 W station does not have a considerably longer up-time, even a 20 W station shows promising results. Both Station 11 and 13 could have been used for about half a month longer. In the future, the local test station at ECAP will be used to compare

power generation data from the wind turbine with that from the RNO-G stations. From this, valuable insight into how the turbine performs under less harsh conditions can be gained. This will hopefully also clear up why the turbine sometimes generates less power than it should. In order to do so, some malfunctions of the data bus of the ECAP station need to be fixed, which unfortunately were not repairable in the limited time of this thesis. Also, the Ethernet cable, tethering the station to the ECAP, will be replaced by an LTE modem in the future. This not only allows for the relocation of the station if need be, but also enables researchers not employed by the ECAP itself to communicate and work with the system.

The second research focus of gathering insight into wind-related background signals starts, as did the first one, with building an experimental setup. The objective is to connect a glaciophone to a Raspberry Pi-4 and record acoustic signals in the vicinity of an RNO-G station, in the hopes of relating these to heightened trigger rates of the detector during periods with strong wind. For this, the Raspberry Pi is equipped with an AD HAT by Waveshare [31]. This add-on component sports an ADS1263 ADC from Texas Instruments [32]. The power is supplied by a 12 V lead-acid battery, and the necessary voltages are generated with DC-DC converters as well as voltage dividers. Capacitors are used to filter the differential signal inputs from the glaciophone. This setup needed to be constructed and tested very quickly for it to be flown to Greenland with the next available plane; therefore, no calibration was achieved. In the field, the equipment was deployed in anticipation of high wind speeds by Felix Schlüter and Jason Chan. The glaciophone was buried about 0.5 m deep into the snow near station 13, while the enclosure housing the electronics was placed on a wooden plank. Due to the battery needing to be recharged, two separate runs were performed. In the first one, the electronics were additionally covered with a plastic bag, which was deemed unnecessary in the second run. After recovery, the data was read out and analysed. The first run (31.05.2025 - 15:48 to 06.06.2025 - 17:47) demonstrates greatly the effect wind can have on the detector. As the wind speed rises to about 15 m/s, the trigger rate of station 13 spikes to approximately 18 times the normal rate. While the acoustic noise increases simultaneously with the wind speed (with a Pearson coefficient of 0.762), the trigger rate exhibits a significant delay of around 6 h. A Pearson coefficient of ± 1 would suggest maximum linear correlation, while 0 signifies no linear correlation. The Pearson coefficient between the trigger rate and the wind speed is 0.535. This shows a relatively good correlation in the first run. However, between the trigger rate and the acoustic noise, the coefficient is reduced to 0.300, suggesting these variables are still correlated, but less so. The second run, however, showed no correlation between the trigger rate and either wind speed or acoustic noise. This may be attributed to the lower wind velocity (below 10 m/s). In conclusion, even though the wind speed alone is not a perfect indicator of wind-related background signals, it seems to have a higher prediction power than acoustic noise. Since the first run was done with a plastic bag covering the electronics, the frequency plot is compromised, as this introduces artificial noise. During the second run, no spike in the trigger rate was recorded. The most insight would be gathered from a run where a spike is observed while only the potential acoustic noise related to the triboelectric is recorded. If possible, the tests should be run again during high winds above 10 m/s. The mystery of why the triggerates do not spike simultaneously with the wind speed but on average 2.8 h later, is still unsolved and requires further investigation. More research is also required to answer the question

of why the trigger rate is only sometimes affected by wind.

Both experiments are paving the way for future endeavours. The first part shows that a station consuming less power should be the highest priority to increase up-time. Tests of a larger WT14 turbine have already begun and are showing promising results. All the while, reducing power consumption of all electrical systems is an ongoing project in the RNO-G collaboration. The new turbine could double power generation from wind, making it possible to switch on the detector stations during high wind periods intermittently. However, for this to be possible, the increased background noise from wind-related events needs to be understood and, if possible, eliminated or reduced. As both the wind speed and the acoustic noise do not present a perfect correlation to the trigger rates of the detector, other factors must play a role. This may be as simple as including the direction of the wind in the evaluation or a much more complicated aspect of the triboelectric effect, which is not entirely understood yet.

With higher power generation and lower power consumption, there is a longer up-time. Pairing this with reduced background noise is crucial to achieve the sensitivity goal for the RNO-G project.

A Appendix

A.1 Power Data - Station 11

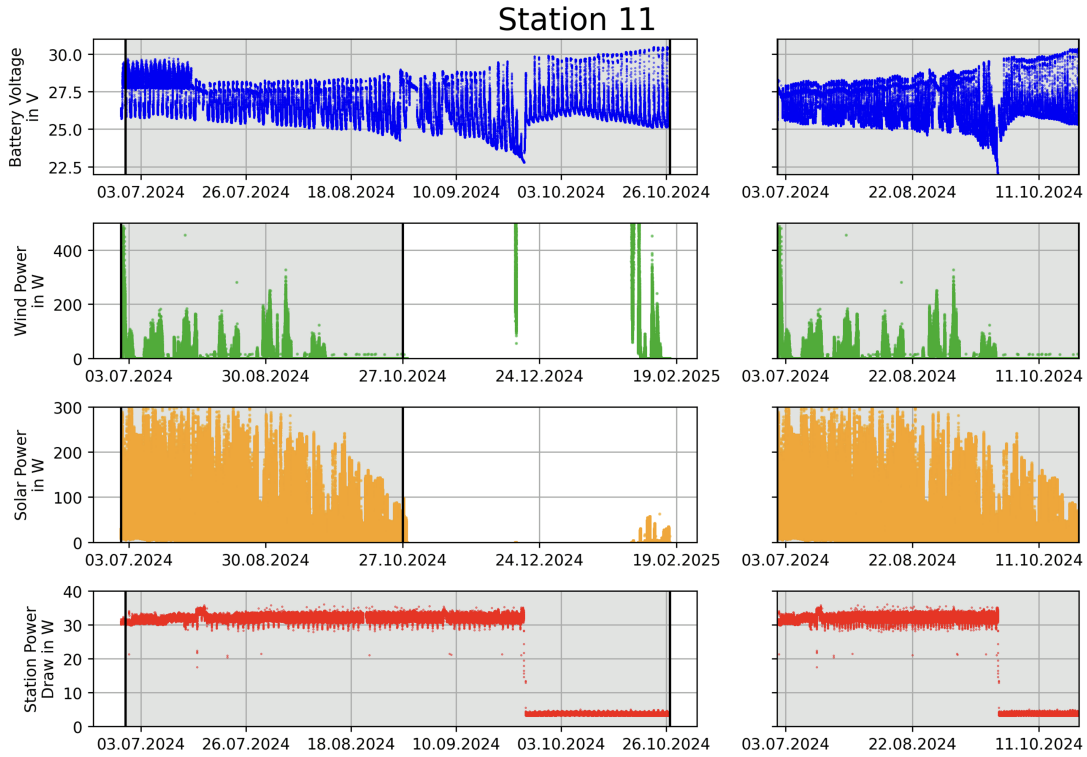

Figure 48: Overview of the available data for station 11. The area marked in gray shows a time interval in which there is no interruption of the data of any varaible.

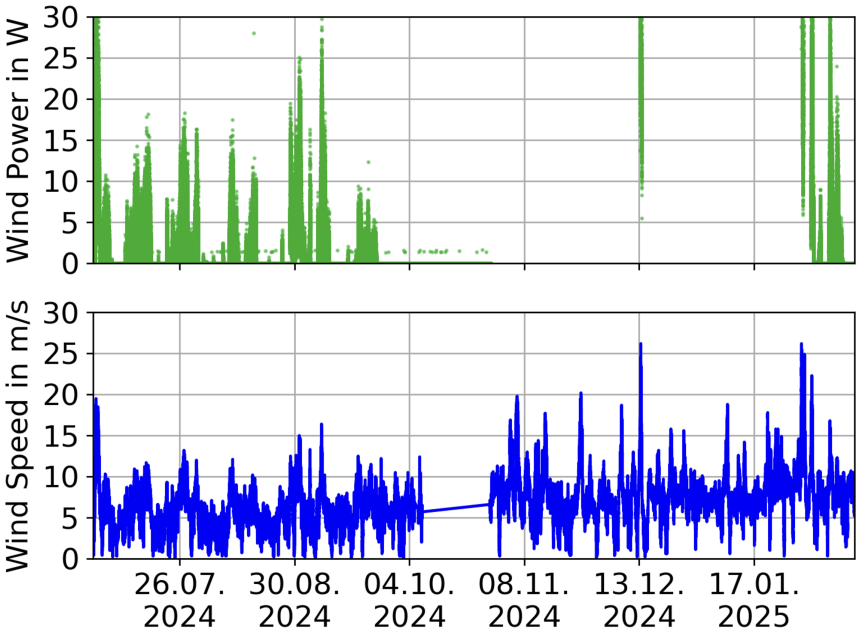

Figure 49: Wind power delivered by the WT10 turbine on station 11 (top) and available wind speed data from Summit station at the time (bottom). The wind speed is measured every 60 s while the station's power readings are updated every 20 s

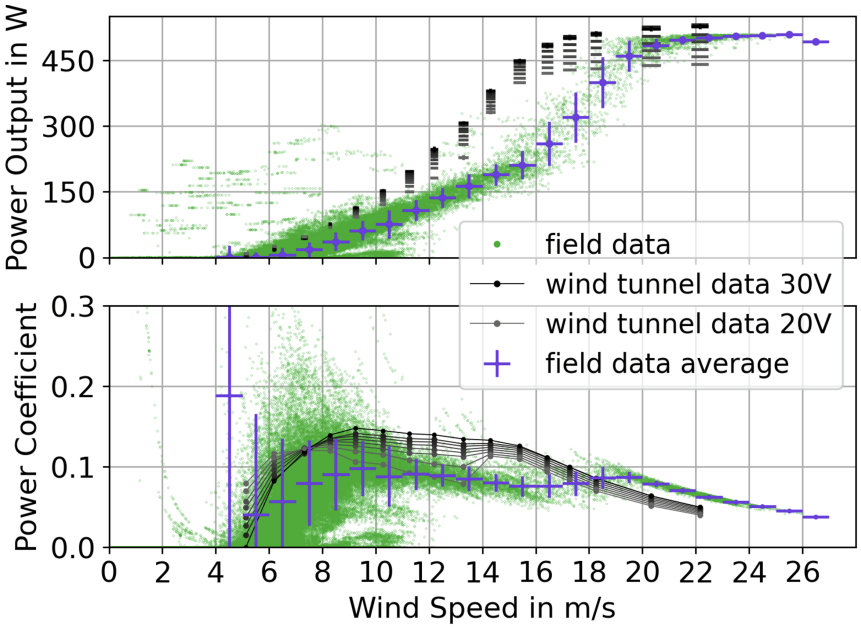

Figure 50: Data from Station 11. Top: Power output of the turbine. Bottom: Power efficiency coefficient of the turbine depending on wind speed. Both plots feature the raw data and the median, with the 16th and 84th percentiles. The expected values from the wind tunnel test are included as well. The power coefficient is calculated as described in equation 8. The power data is averaged across 5 minutes (15 data points) to achieve a more precise measurement.

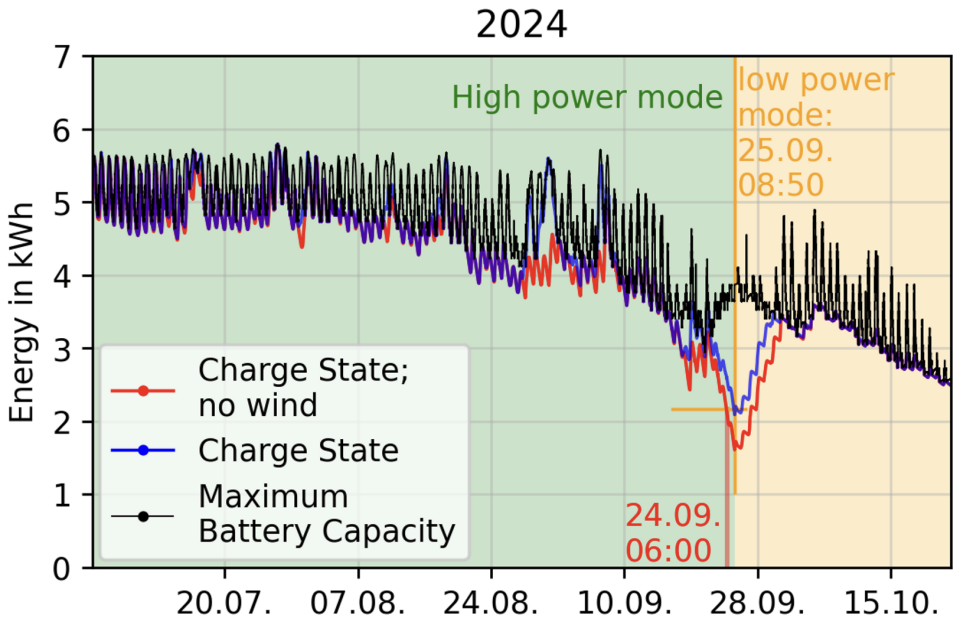

Figure 51: Battery capacity and charge state are calculated with equations 19 and 22 based on the input and output power as well as the temperature measured inside the battery compartment from station 11. Similarly, the theoretical charge state without wind power is calculated by removing P_{Wind} from P_{eff} in equation 22. Marked in red is one instances where the station would need to be switched to low power mode without wind power.

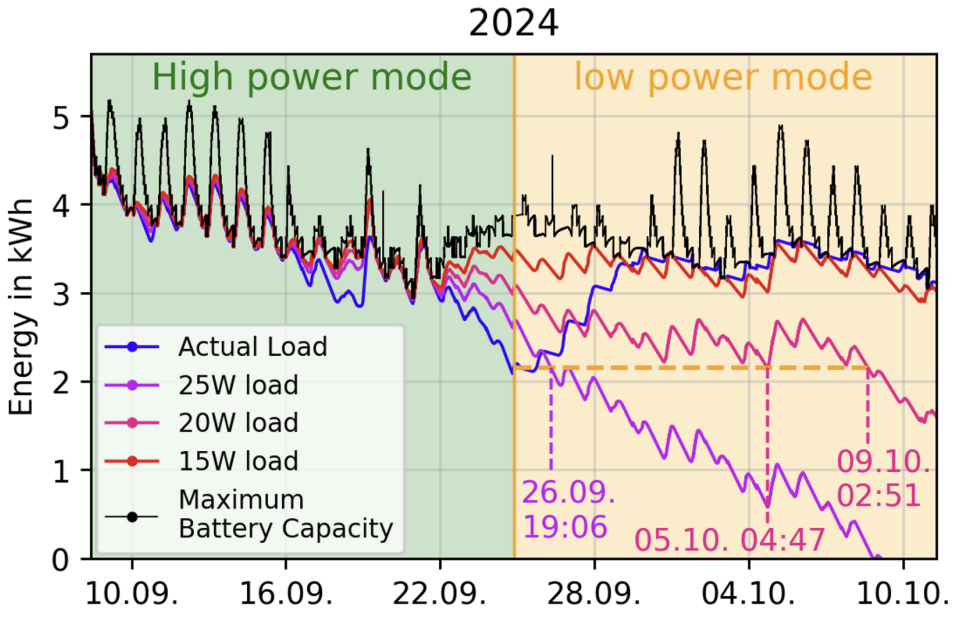

Figure 52: Comparing simulated power draw of 25 W, 20 W, and 15 W to the real data of station 11. For 25 W and 20 W, the dates when they would switch to low power mode are marked.

A.2 Power Data - Station 12

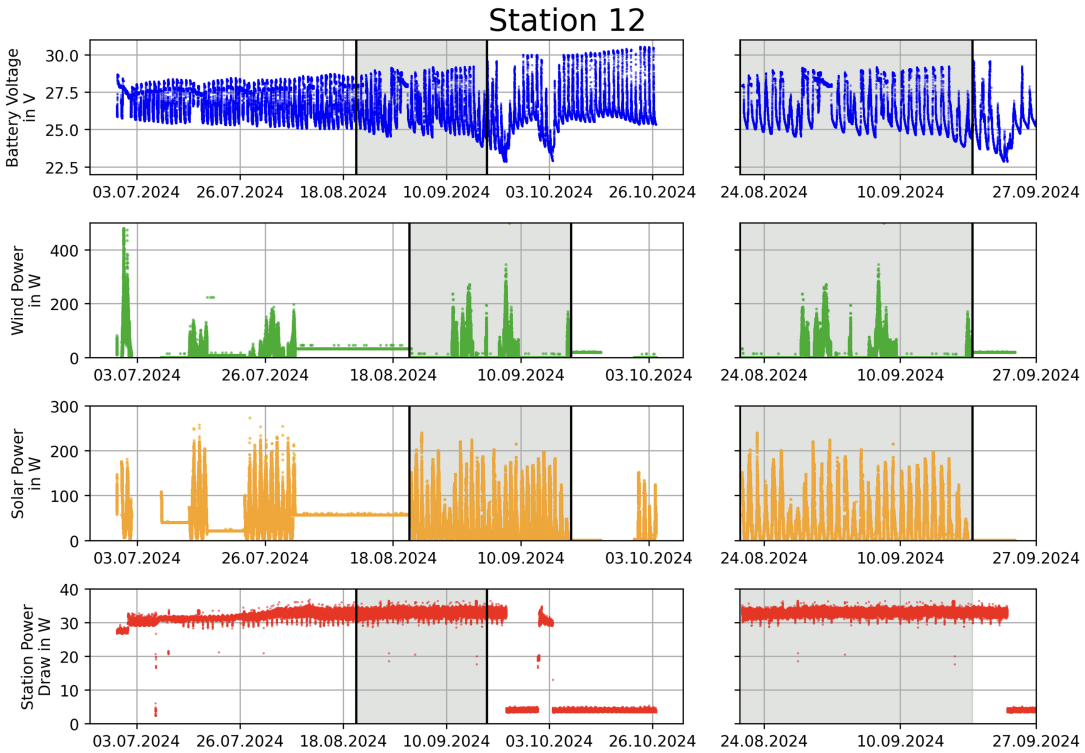

Figure 53: Overview of the available data for station 12. The area marked in gray shows a time interval in which there is no interruption of the data of any variable.

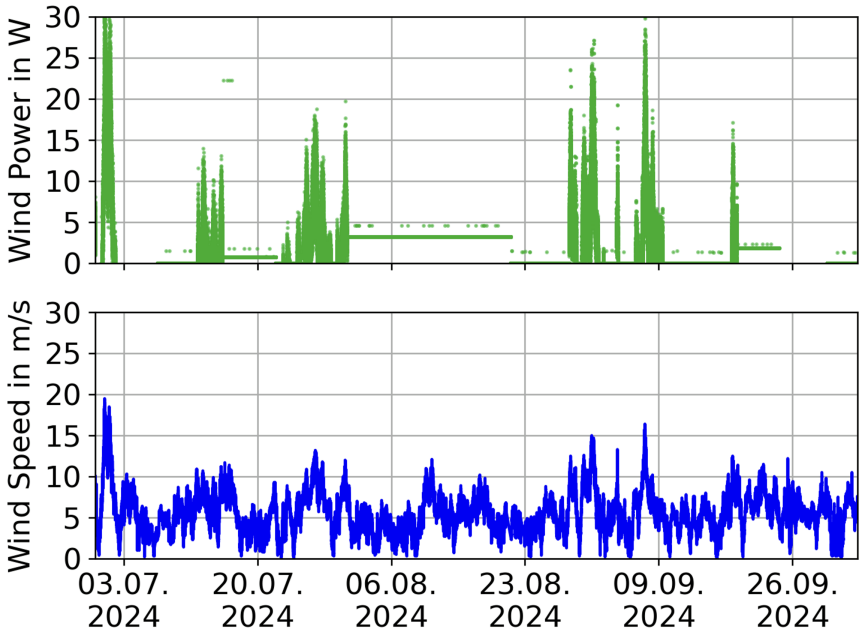

Figure 54: Wind power delivered by the WT10 turbine on station 12 (top) and available wind speed data from Summit station at the time (bottom). The wind speed is measured every 60 s while the station's power readings are updated every 20 s

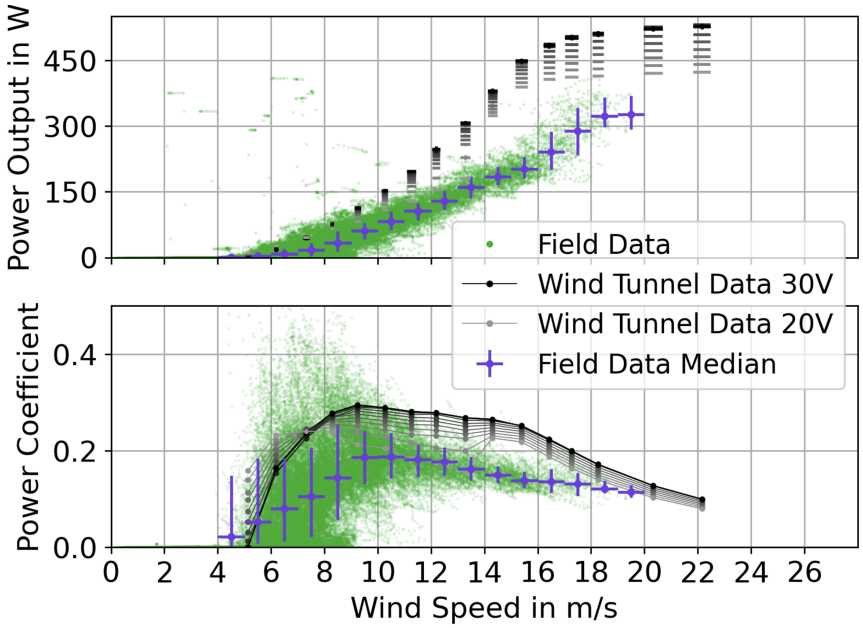

Figure 55: Data from station 12. Top: Power output of the turbine. Bottom: Power efficiency coefficient of the turbine depending on wind speed. Both plots feature the raw data and the median, with the 16th and 84th percentiles. The expected values from the wind tunnel test are included as well. The power coefficient is calculated as described in equation 8. The power data is averaged across 5 minutes (15 data points) to achieve a more precise measurement.

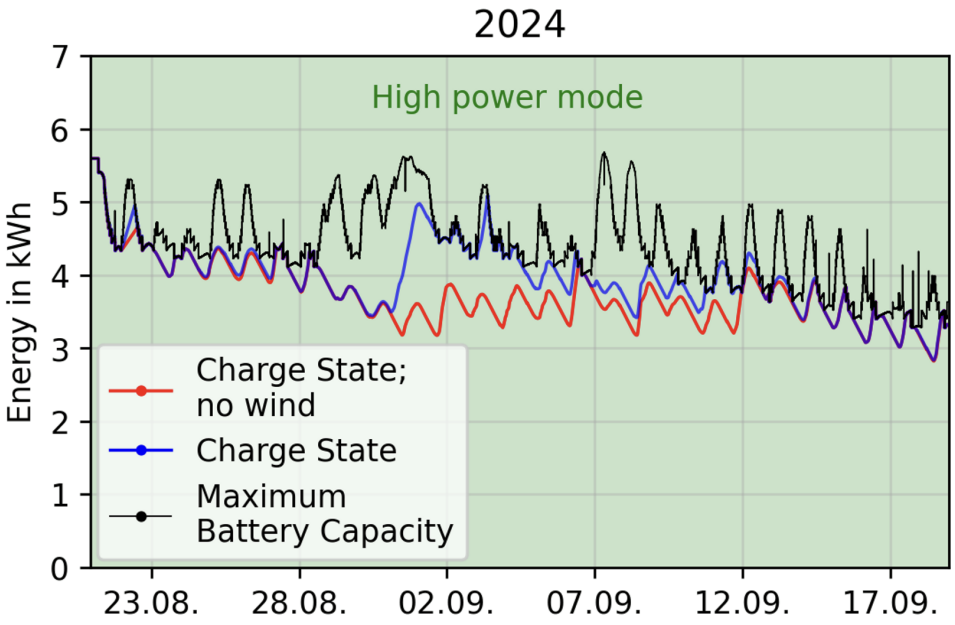

Figure 56: Battery capacity and charge state are calculated with equations 19 and 22 based on the input and output power as well as the temperature measured inside the battery compartment from station 12. Similarly, the theoretical charge state without wind power is calculated by removing P_{Wind} from P_{eff} in equation 22.

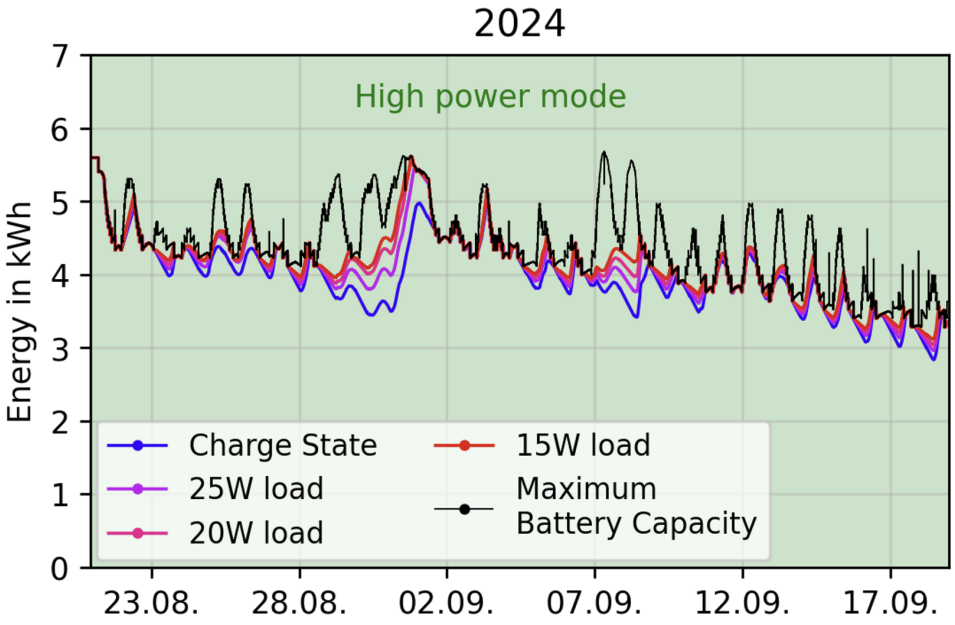

Figure 57: Comparing simulated power draw of 25 W, 20 W, and 15 W to the real data of station 12. For 25 W and 20 W, the dates when they would switch to low power mode are marked.

A.3 Power Data - Station 14

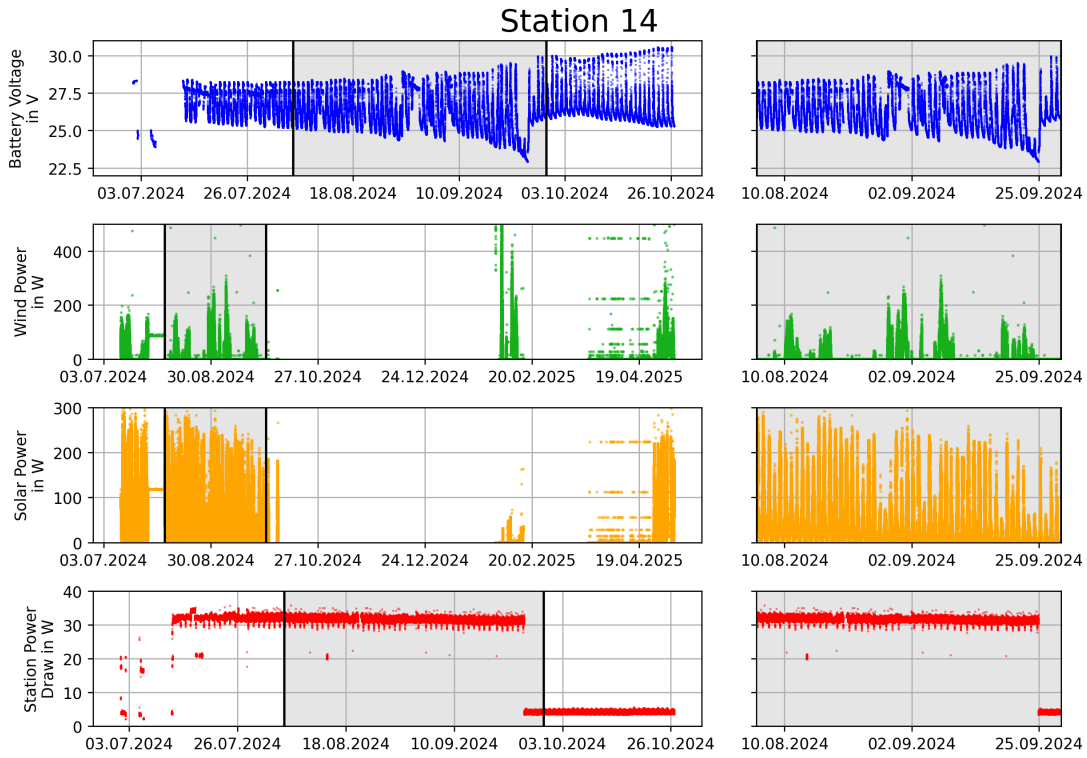

Figure 58: Overview of the available data for station 14. The area marked in gray shows a time interval in which there is no interruption of the data of any variable.

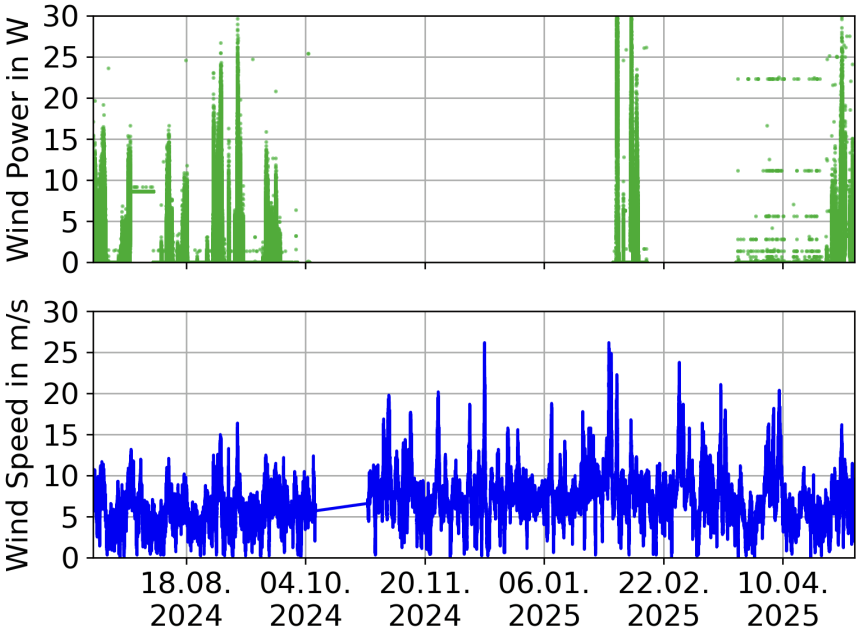

Figure 59: Wind power delivered by the WT10 turbine on station 14 (top) and available wind speed data from Summit station at the time (bottom). The wind speed is measured every 60 s while the station's power readings are updated every 20 s

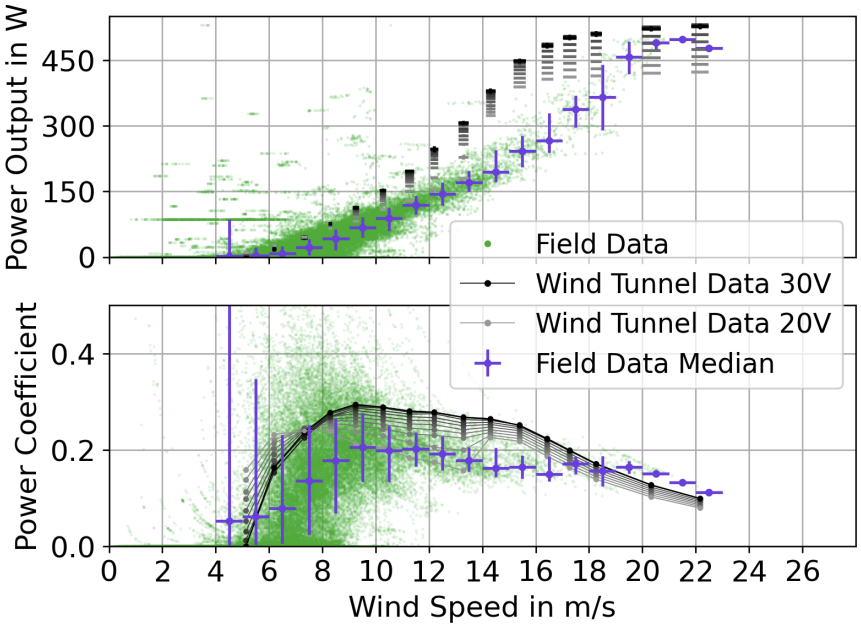

Figure 60: Data from station 14. Top: Power output of the turbine. Bottom: Power efficiency coefficient of the turbine depending on wind speed. Both plots feature the raw data and the median, with the 16th and 84th percentiles. The expected values from the wind tunnel test are included as well. The power coefficient is calculated as described in equation 8. The power data is averaged across 5 minutes (15 data points) to achieve a more precise measurement.

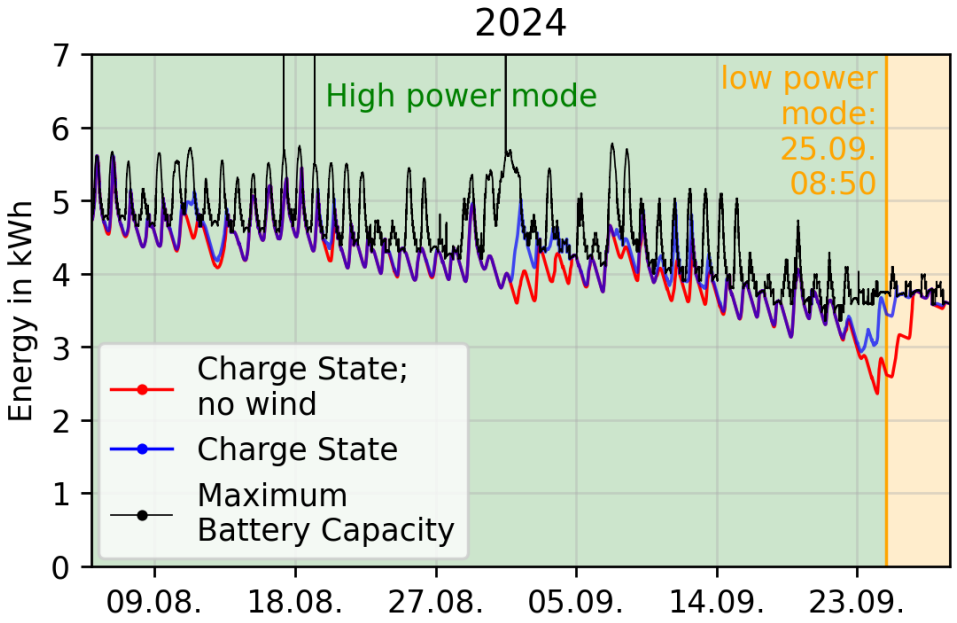

Figure 61: Battery capacity and charge state are calculated with equations 19 and 22 based on the input and output power as well as the temperature measured inside the battery compartment from station 14. Similarly, the theoretical charge state without wind power is calculated by removing P_{Wind} from P_{eff} in equation 22.

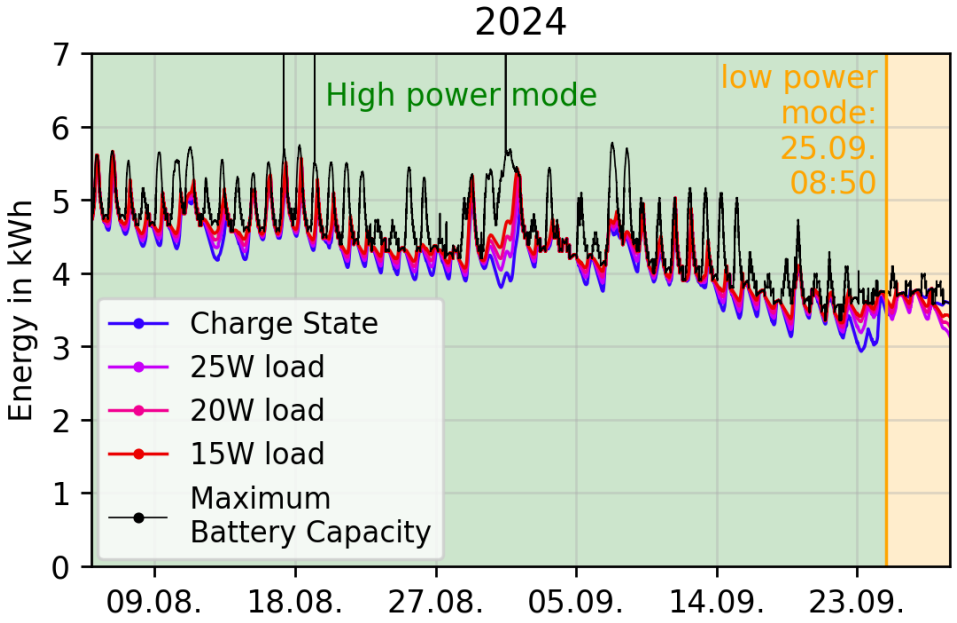

Figure 62: Comparing simulated power draw of 25 W, 20 W, and 15 W to the real data of station 14. For 25 W and 20 W, the dates when they would switch to low power mode are marked.

A.4 Power Data - Station 23

Due to the low amount of data from station 23, a simulation of the battery charge state could not be accomplished.

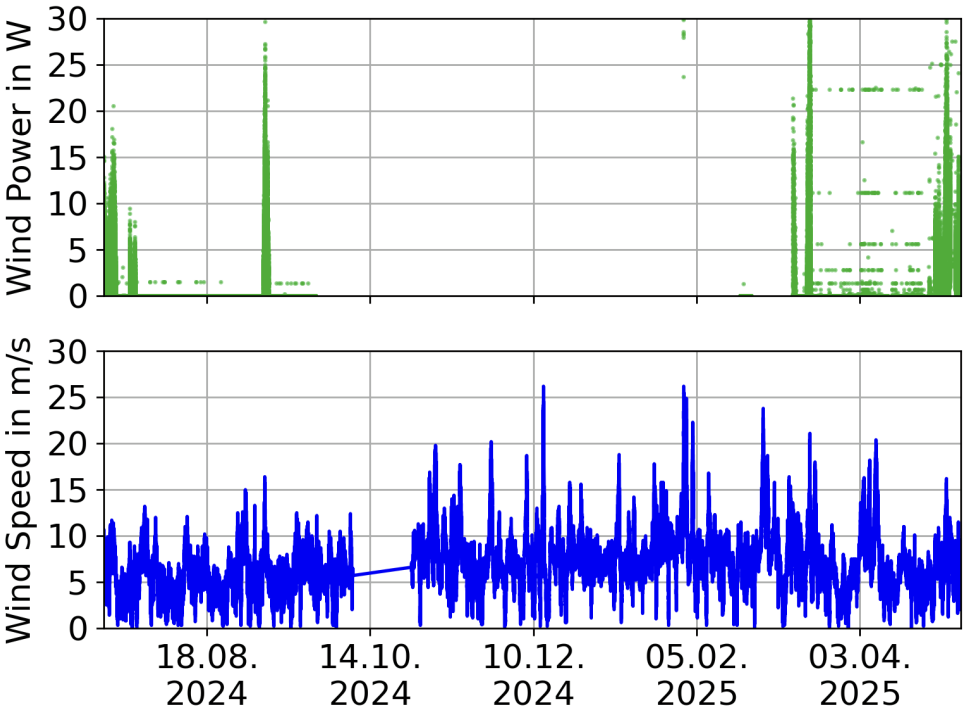

Figure 63: Wind power delivered by the WT10 turbine on station 23 (top) and available wind speed data from Summit station at the time (bottom). The wind speed is measured every 60 s while the station's power readings are updated every 20 s

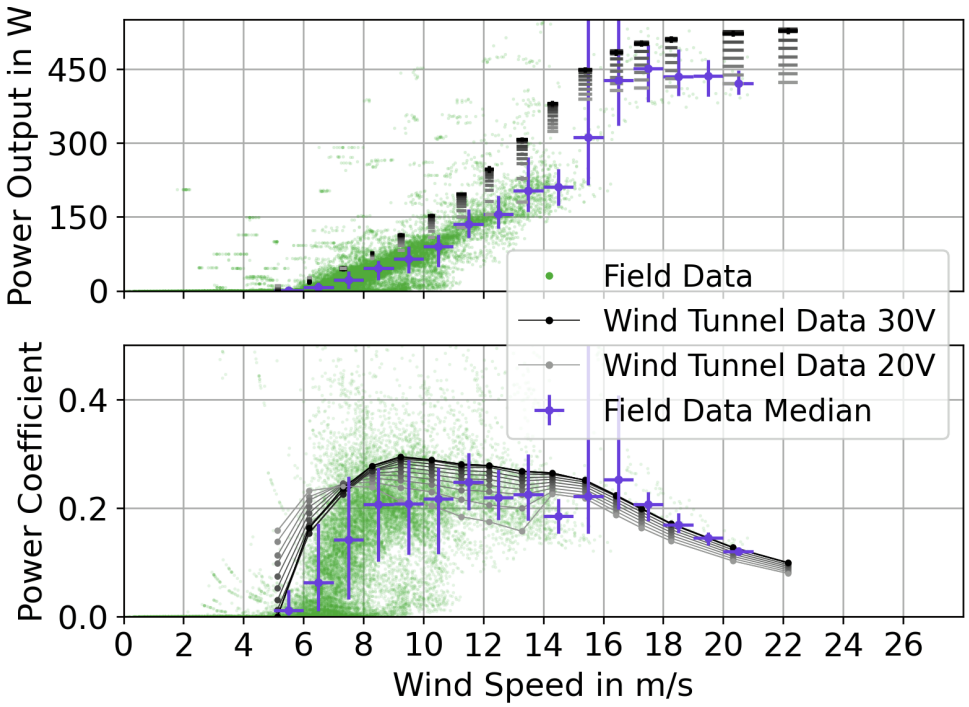

Figure 64: Data from station 23. Top: Power output of the turbine. Bottom: Power efficiency coefficient of the turbine depending on wind speed. Both plots feature the raw data and the median, with the 16th and 84th percentiles. The expected values from the wind tunnel test are included as well. The power coefficient is calculated as described in equation 8. The power data is averaged across 5 minutes (15 data points) to achieve a more precise measurement.

Bibliography

[1] Lyndon Evans. "The Large Hadron Collider". In: *Annual Review of Nuclear and Particle Science, 61, 435-466* (2011). URL: https://doi.org/10.1146/annurev-nucl-102010-130438.

[2] Luke O'C Drury. "An introduction to the theory of diffusive shock acceleration of energetic particles in tenuous plasmas". In: *Reports on Progress in Physics* 46.8 (1983), p. 973. DOI: 10.1088/0034-4885/46/8/002. URL: https://doi.org/10.1088/0034-4885/46/8/002.

[3] Ellen G. Zweibel and Masaaki Yamada. "Magnetic Reconnection in Astrophysical and Laboratory Plasmas". In: *Annual Review of Astronomy and Astrophysics* 47.Volume 47, 2009 (2009), pp. 291–332. ISSN: 1545-4282. DOI: https://doi.org/10.1146/annurev-astro-082708-101726. URL: https://www.annualreviews.org/content/journals/10.1146/annurev-astro-082708-101726.

[4] Lilly Marie Pyras. "Cosmic Rays and the Radio Neutrino Observatory Greenland (RNO-G)". PhD thesis. Naturwissenschaftlichen Fakultät der Friedrich-Alexander-Universität Erlangen-Nürnberg, 2024.

[5] National Science Foundation (NSF). *Summit Station*. URL: https://geo-summit.org/summit-station.

[6] National Oceanic and Atmospheric Administration. *Global Monitoring Laboratory - Meteorology*. URL: https://gml.noaa.gov/aftp/data/meteorology/in-situ/sum/ (visited on 04/09/2025).

[7] ATLAS Open Data. *The Standard Model of Particle Physics and Beyond*. URL: https://opendata.atlas.cern/docs/documentation/introduction/SM_and_beyond/ (visited on 03/07/2025).

[8] Sjoerd Bouma. "Direction Reconstruction of Radio Signals in Neutrino Detectors in Ice". PhD thesis. Naturwissenschaftlichen Fakultät der Friedrich-Alexander-Universität Erlangen-Nürnberg, 2025.

[9] Frank G. Schröder. "Radio detection of cosmic-ray air showers and high-energy neutrinos". In: *Progress in Particle and Nuclear Physics* 93 (2017), pp. 1–68. ISSN: 0146-6410. DOI: https://doi.org/10.1016/j.ppnp.2016.12.002. URL: https://www.sciencedirect.com/science/article/pii/S0146641016300758.

[10] Anne Zilles. "Emission of Radio Waves in Particle Showers: Validation of microscopic simulations with the SLAC T-510 experiment and their potential in the future Square Kilometre Array". 51.03.04; LK 01. PhD thesis. Karlsruher Institut für Technologie (KIT), 2016. 118 pp. DOI: 10.5445/IR/1000065046.

[11] G A Askaryan. "EXCESS NEGATIVE CHARGE OF AN ELECTRON-PHOTON SHOWER AND THE COHERENT RADIO EMISSION FROM IT". In: *Zhur. Eksptl'. i Teoret. Fiz.* Vol: 41 (Aug. 1961). URL: https://www.osti.gov/biblio/4833087.

[12] S. Agarwal et al. "Instrument design and performance of the first seven stations of RNO-G". In: *Journal of Instrumentation* 20.04 (2025), P04015. DOI: 10.1088/

1748-0221/20/04/P04015. URL: https://doi.org/10.1088/1748-0221/20/04/P04015.

[13] Ameresco Solar. *120W (24V) Photovoltaic Module 120JB-V Datasheet*. URL: https://www.amerescosolar.com/wp-content/uploads/Ameresco-Solar-120JB-V-2021.pdf.

[14] Ameresco Solar. *180W (24V) Photovoltaic Module 180J-V Datasheet*. URL: https://www.amerescosolar.com/wp-content/uploads/Ameresco-Solar-180J-V-2021.pdf.

[15] Anna Nelles. "A wind-turbine for autonomous stations for radio detection of neutrinos". In: *PoS* ICRC2019 (2019), p. 968. DOI: 10.22323/1.358.0968.

[16] Phaesun. *Sun Plus Solar Modules Datasheet*. URL: https://asset.conrad.com/media10/add/160267/c1/-/de/001590111DS01/datenblatt-1590111-phaesun-sun-plus-100-polykristallines-solarmodul-100-wp-24-v.pdf.

[17] LLC APRS World. *WT10: 1.0 meter Micro Wind Turbine*. URL: http://www.aprsworld.com/wtaprs/WT10/.

[18] Stadt Erlangen. *Statistik: Wetter und Klima*. URL: https://erlangen.de/aktuelles/wetterstatistik (visited on 04/12/2024).

[19] Deka Solar. *Deka Solar 8G31-HST-DEKA Sealed Gel Cell Battery spec sheet*. URL: https://www.solarelectricsupply.com/deka-8g31solar-batteries (visited on 06/29/2025).

[20] CTM Berlin. *Overview CTV Batteries*. URL: https://www.ctm-berlin.de/wp-content/uploads/2021/04/CTV-Reihe-Uebersicht_Gebrauchsanweisung.pdf (visited on 10/17/2025).

[21] DuraSat. *DUR-line Herkules 8PL XL 1,7m - 8-Plattenständer*. URL: https://www.durasat.de/Montagematerial/Balkon-und-Flachdachmontage/DUR-line-Herkules-8PL-XL-1-7m-8-Plattenstaender-Mast-1-7m.html (visited on 10/20/2025).

[22] TriStar. *Solar Charging System Controller - Installation, Operation and Maintenance Manual*. URL: https://www.solar-electric.com/lib/wind-sun/TriStar-manual.pdf.

[23] Gao X. Meng-K. Qiu-J. Lai L. L. Gao S. Wang D. "Utilisation of kinetic energy from wind turbine for grid connections: A review paper". In: *IET Renewable Power Generation, 12(6), 615-624* (2018). URL: https://doi.org/10.1049/iet-rpg.2017.0590.

[24] National Oceanic and Atmospheric Administration. *Air Pressure*. URL: https://www.noaa.gov/jetstream/atmosphere/air-pressure (visited on 10/02/2025).

[25] Donald P. Gatley, Sebastian Herrmann, and Hans-Joachim Kretzschmar. "A Twenty-First Century Molar Mass for Dry Air". In: *HVAC&R Research* 14.5 (2008), pp. 655–662. DOI: 10.1080/10789669.2008.10391032. URL: https://doi.org/10.1080/10789669.2008.10391032.

[26] Richard Shelquist. *An Introduction to Air Density and Density Altitude Calculations*. URL: https://wahiduddin.net/calc/density_altitude.htm.

[27] George Clarke Simpson. *British Antarctic Expedition 1910–1913: Meteorology*. Thacker, Spink co, 1919. DOI: https://doi.org/10.5962/bhl.title.6801.

[28] Juan Antonio Aguilar et al. "Triboelectric backgrounds to radio-based polar ultra-high energy neutrino (UHEN) experiments". In: *Astroparticle Physics* 145 (2023), p. 102790. ISSN: 0927-6505. DOI: https://doi.org/10.1016/j.astropartphys.2022.102790. URL: https://www.sciencedirect.com/science/article/pii/-S0927650522000913.

[29] Inc. High Tech. *HTI-92-WB*. URL: https://www.hightechincusa.com/products/hydrophones/hti92wb.html (visited on 10/14/2025).

[30] J.A. Aguilar et al. "AMADEUS—The acoustic neutrino detection test system of the ANTARES deep-sea neutrino telescope". In: *Nuclear Instruments and Methods in Physics Research Section A: Accelerators, Spectrometers, Detectors and Associated Equipment* 626–627 (Jan. 2011), 128–143. ISSN: 0168-9002. DOI: 10.1016/j.nima.2010.09.053. URL: http://dx.doi.org/10.1016/j.nima.2010.09.053.

[31] Waveshare. *High-Precision AD HAT*. URL: https://www.waveshare.com/wiki/High-Precision_AD_HAT (visited on 10/14/2025).

[32] Texas Instruments. *ADS1263*. URL: https://www.ti.com/product/de-de/ADS1263 (visited on 10/14/2025).

[33] Seacon. *All-Wet underwater electrical wet-mate connectors*. URL: https://www.te.com/content/dam/te-com/documents/aerospace-defense-and-marine/SEACON/seacon-all-wet-brochure.pdf (visited on 10/14/2025).

[34] Emiel Por, Maaike Van Kooten, and Vanja Sarkovic. "Nyquist-Shannon sampling theorem". In: *Leiden University* 1.1 (2019), pp. 1–2.

[35] PennState Eberly College of Science. *Lesson 2: Simple Linear Regression (SLR) Model - 2.6 - (Pearson) Correlation Coefficient r*. URL: https://online.stat.psu.edu/stat462/node/96/ (visited on 10/02/2025).

Acknowledgements

First of all, I would like to express my thanks to my supervisor, Prof. Dr. Anna Nelles. Being both independent in determining the direction of the project as well as having structured guidance to fall back on has been an invaluable experience. I would also like to express my appreciation for the opportunities she provided me with, including connecting me with other scientists, as well as for valuing my expertise for other projects.

I also want to thank the researchers and staff at the ECAP and the RNO-G collaboration for aiding me in furthering my knowledge of electronics, manufacturing, and mathematics, and for providing insight into the workings of RNO-G and its detector stations. These thanks go to, in no particular order, Dr. Adrian Zink, Dr. Kay Graf, Dr. Timo Karg, Prof. Dr. Robert Lahmann, Dr. Philipp Windischhofer, Nils Heyer and Dr. Felix Schlüter. Special thanks go to Felix Schlüter and Jason Chan for deploying the acoustic measuring equipment in the bitterly cold environment of Greenland.

On that note, I would also like to show my highest appreciation to those who helped me move all the heavy equipment to the ECAP roof on one of the hottest summer days.

Last but certainly not least, I am incredibly thankful for the love, motivation and unconditional support of my family and friends.

Declaration of Originality

I, Pascal Schriefer, student registration number: 22677162, hereby confirm that I completed the submitted work independently and without the unauthorized assistance of third parties and without the use of undisclosed and, in particular, unauthorized aids. This work has not been previously submitted in its current form or in a similar form to any other examination authorities and has not been accepted as part of an examination by any other examination authority.

Where the wording has been taken from other people's work or ideas, this has been properly acknowledged and referenced. This also applies to drawings, sketches, diagrams and sources from the Internet.

In particular, I am aware that the use of artificial intelligence is forbidden unless its use and aid has been expressly permitted by the examiner. This applies in particular to chatbots (especially ChatGPT) and such programs in general that can complete the tasks of the examination or parts thereof on my behalf.

Any infringements of the above rules constitute fraud or attempted fraud and shall lead to the examination being graded "fail" ("nicht bestanden").

Place, Date	Signature